Universidade Federal de Santa Catarina
Centro Tecnológico, de Ciências Exatas e Educação
Engenharia de Materiais - Campus Blumenau

Jaquelline Vanelli

Investigation of the copper grain size influence on the achievable structure resolution and quality in nanoscale direct ablation using ultrashort pulsed laser radiation

Blumenau
2022

Jaquelline Vanelli

Investigation of the copper grain size influence on the achievable structure resolution and quality in nanoscale direct ablation using ultrashort pulsed laser radiation

Final paper submitted in partial fulfillment of the requirements for the degree of BEng. in Materials Engineering of the Universidade Federal de Santa Catarina.
Advisor: Prof. Dr. Milton Pereira

Universidade Federal de Santa Catarina
Centro Tecnológico, de Ciências Exatas e Educação
Engenharia de Materiais - Campus Blumenau

Blumenau
2022

Vanelli, Jaquelline
Investigation of the copper grain size influence on the achievable structure resolution and quality in nanoscale direct ablation using ultrashort pulsed laser radiation / Jaquelline Vanelli; orientador, Prof. Dr. Milton Pereira, 2022.
70 p.

Trabalho de Conclusão de Curso (graduação) - Universidade Federal de Santa Catarina, Campus Blumenau, Graduação em Engenharia de Materiais, Blumenau, 2022.

Inclui referências.

1. Engenharia de Materiais. 2. Laser material processing. 3. Ultrashort laser ablation. 4. Grain size determination. 5. Influence of copper grain size. I. Pereira, Milton. II. Universidade Federal de Santa Catarina. Graduação em Engenharia de Materiais. III. Título.

Jaquelline Vanelli

Investigation of the copper grain size influence on the achievable structure resolution and quality in nanoscale direct ablation using ultrashort pulsed laser radiation

Final paper submitted in partial fulfillment of the requirements for the degree of BEng. in Materials Engineering of the Universidade Federal de Santa Catarina.

ICP-Edu
Documento assinado digitalmente
Jaquelline Vanelli
Data: 02/08/2022 12:21:17-0300
CPF: 107.445.329-81
Verifique as assinaturas em https://v.ufsc.br

Jaquelline Vanelli
Student

Examination Committee

ICP-Edu
Documento assinado digitalmente
Milton Pereira
Data: 02/08/2022 12:55:10-0300
CPF: 823.484.489-04
Verifique as assinaturas em https://v.ufsc.br

Prof. Dr. Milton Pereira
Advisor

ICP-Edu
Documento assinado digitalmente
Claudio Abilio da Silveira
Data: 02/08/2022 12:56:51-0300
CPF: 075.716.289-46
Verifique as assinaturas em https://v.ufsc.br

Prof. Dr. Claudio Abilio da Silveira
Universidade Federal de Santa Catarina

ICP-Edu
Documento assinado digitalmente
Manoel Kolling Dutra
Data: 02/08/2022 12:41:33-0300
CPF: 073.766.339-10
Verifique as assinaturas em https://v.ufsc.br

Prof. Dr. Manoel Kolling Dutra
Universidade Federal de Santa Catarina

Blumenau, July 18, 2022

To my teddy bear, Gatto.

Acknowledgements

First of all, I immensely thank the couple from "A grande família", my parents Augustinho and Isabel, who always believed in the transforming power of education and spared no efforts to provide me with what they themselves did not have.

To my brother Brunno, my source of inspiration with whom I shared many memories, my first beer in Germany and we will always have in common duplicate letters in the name for no reason.

To my dynamic college duo, Felipe Michels, who has provided me with many laughs, deep conversations and asked me to calm down more times than I can humanly count, making college a panic-free and much better place to be.

To my life friends Tony, who was also my English and geography teacher, bought my dream and enabled me to achieve it and Maithê for supporting me in any decision and always being a great emotional support.

Thanks to Lara Fernandes, who was my undergraduate research project advisor, for trusting my work in this opportunity that opened many doors and made me love the course and research.

Thanks a lot to my advisor Milton Pereira that more than contributing to the technical and theoretical part of the work, believed in my capacity and encouraged me to finish it.

To my supervisor at the Institute Martin Osbild who was patient and hardworking in hiring a foreigner in the middle of the pandemic, making one of my biggest dreams come true. I also extend my thanks to all the Fraunhofer ILT employees that helped in the experimental part.

To UFSC - Blumenau and all its professors, a public, free and quality university that guaranteed me a degree in engineering without my parents selling our house.

"A persistência é o caminho do êxito."
(Charles Chaplin)

Resumo

Lasers de pulso ultra-curtos são cada vez mais utilizados para o processamento preciso de material pois garantem maior qualidade de ablação. Com o avanço da tecnologia são necessárias resoluções estruturais cada vez mais finas e muito se estuda acerca da influência dos parâmetros do laser na obtenção dessas estruturas, porém, ainda pouco se sabe a respeito da influência das propriedades dos materiais na resolução e qualidade da estrutura alcançável. Como ainda há poucas referências dedicadas à investigação científica sobre estas correlações, a escolha atual de um material para microestruturação a laser de alta resolução é baseada puramente em valores empíricos fenomenológicos. Dentre as várias classes de materiais existentes, bem como suas características intrínsecas, no âmbito deste trabalho de conclusão de curso, o objetivo principal foi avaliar a influência do tamanho do grão do cobre, obtido através de diferentes taxas de resfriamento pós fundição, na resolução e qualidade da estrutura alcançável durante a ablação direta em nanoescala usando radiação laser pulsada ultra-rápida. Utilizou-se 3 diferentes tamanhos de grão sendo eles 10, 525 e 1391 µm, onde foram abladas linhas paralelas variando-se a potência do laser em 5,37; 25,34 e 113,9 mW e também as repetições em cada linha em 5, 15 e 50 vezes. As amostras foram caracterizadas microestruturalmente com um microscópio óptico e morfologicamente com o auxílio de um microscópio eletrônico de varredura (MEV), o qual também contribuiu para a análise de largura das linhas abladas. A profundidade e o perfil da cavidade de ablação foi verificada com o uso de um microscópio confocal de varredura a laser. A partir da análise do conjunto de dados qualitativos e quantitativos, concluiu-se que o aumento da densidade dos contornos de grão possui, assim como na resistência mecânica e condutividade elétrica, atua como barreiras para a transferência da energia do laser no interior do material, dissipando parte dessa energia devido a sua reatividade e causando menos dano no material. Esse fenômeno faz com que o cobre com menor tamanho de grão auxilie na formação de estruturas mais uniformes e com melhor qualidade na ablação a laser ultra-rápida.

Palavras-Chave: 1. Ablação. 2. Cobre. 3. Laser. 4. Tamanho de grão. 5. Ultra-curto

Abstract

Ultrashort pulse lasers are increasingly used for precise material processing as they ensure a higher quality of ablation. With the advancement of technology, finer structural resolutions are required and much has been studied about the influence of laser parameters in obtaining these structures, but little is known about the influence of material properties on the resolution and quality of the achievable structure. As there are still few references dedicated to scientific research on these correlations, the current choice of a material for high-resolution laser microstructuring is based purely on empirical phenomenological values. Among the various existing classes of materials, as well as their intrinsic characteristics, in the scope of this bachelor's thesis, the main objective was to evaluate the influence of copper grain size, obtained through different post-casting cooling rates, on the resolution and quality of the structure achievable during direct nanoscale ablation using ultrafast pulsed laser radiation. Three different grain sizes were used, namely 10, 525 and 1391 µm, where parallel lines were ablated by varying the laser power in 5,37; 25,34 and 113,9 mW and also the repetitions in each line in 5, 15 and 50 times. The samples were characterized microstructurally with an optical microscope and morphologically with the aid of a scanning electron microscope (SEM), which also contributed to the analysis of the width of the ablated lines. The depth and profile of the ablation cavity was verified using a confocal laser scanning microscope (CLSM). From the analysis of the qualitative and quantitative data set, it was concluded that the increase in the density of the grain contours possessed, as well as in the mechanical strength and electrical conductivity, acts as barriers for the transfer of laser energy inside the material, dissipating part of this energy due to its reactivity and causing less damage to the material. This phenomenon makes copper with smaller grain size help in the formation of more uniform structures and with better quality in ultrafast laser ablation.

Keywords: 1. Ablation. 2. Copper. 3. Grain size. 4. Laser. 5. Ultrashort.

List of figures

List of tables

Acronyms

1S	*Small grain size sample*
2M	*Medium grain size sample*
3B	*Big grain size sample*
ASTM	*American Society for Testing and Materials*
B	*Bottom*
CB	*Conduction Band*
CLSM	*Confocal Laser Scanning Microscope*
CPA	*Chirped Pulse Amplification*
EDM	*Electrical Discharge Machining*
FIB	*Focused Ion Beam*
GI	*Gießerei-Institut*
ILT	*Fraunhofer-Institut für Lasertechnik*
ISO	*International Organization for Standardization*
M	*Middle*
M.	*Mensure 1, 2, 3...*
MEV	*Microscópio Eletrônico de Varredura*
MPI	*Multi-Photon Ionization*
RWTH	*Rheinisch-Westfälische Technische Hochschule*
SEM	*Scanning Electron Microscope*
T	*Top*
UFSC	*Universidade Federal de Santa Catarina*
USLP	*Ultrashort Laser Pulsed*
VB	*Valence Band*

Symbols

s	*Second*
ns	*Nanosecond* ($1ns = 10^{-9}s$)
ps	*Picosecond* ($1ps = 10^{-12}s$)
fs	*Femtosecond* ($1fs = 10^{-15}s$)
cm	*Centimetre*
mm	*Millimetre* ($1mm = 10^{-1}cm$)
µm	*Micrometer* ($1\mu m = 10^{-5}cm$)
nm	*Nanometre* ($1nm = 10^{-8}cm$)
F_{th}	*Threshold fluence*
F_0	*Maximum laser fluence*
D	*Diameter of the ablated crater*
R_0	*Initial radius of the plume*
R_c	*Contact front between the plume and the environment*
R_{0c}	*Speed of the plume* R_{0c}
R_{sw}	*External shock wavefront*
R_i	*Internal shock wave propagates inwards*
E	*Purely thermal energy*
G	*ASTM grain size number*
L_{mm}	*Measured grain size in millimeters*
rpm	*Revolutions per minute*
K	*Kelvin*
W	*Watt*
°C	*Celsius degrees*
N	*Newton*
Hz	*Hertz*
HCl	*Hydrochloric acid*
$FeCl_3$	*Iron III chloride*
$(NH_4)_2CuCl_4$	*Diammonium tetrachlorochlorocuprate (II)*
#	*Mesh*

Table of contents

1 Introduction

With its theory based on Einstein's studies and being developed for the first time by Maiman in 1960, the laser tools can be considered one of the greatest innovations of the twentieth century. Due to the versatility of its pure and concentrated energy, lasers have great potential for application both in research and industry and can be used for cutting, welding, drilling, and surface treatments, among others [11].

With a variation of its parameters as the power, for example, the laser beams can be applied since the common daily use of an office as in telecommunications, data storage, printing and recording using low power lasers, as well as in large armaments industries, welding, surgeries and particle acceleration [11].

Since their emergence, lasers have been improved over the years and are currently capable of covering the entire spectral range, becoming easier to use and cheaper with each year of development [1]. Laser ablation is basically a material removal process with nano, pico, ato or femtosecond laser incidence [6] and has been used for drilling micro molds, cleaning surfaces, as well as other small and functional components in electronics [2] as it exhibits good surface finish and aspect ratio when machining, including hard materials [6].

This ability of ultrashort lasers to deposit large amounts of energy in small regions of their targets enables selective modifications in materials, which open up the scope for in-depth investigation of the behavior of their properties under extreme processing conditions [6], as they also exhibit better control and precision in modifying materials than the use of longer pulses [7].

However, although the control of laser beam parameters, beam shaping, and the dynamics of the process itself have well-known effects, the properties of substrate materials have been little explored and have not kept up with this development. As the current choice of materials is based on empirical values, the quality and resolution results may be limited by these properties.

Numerous strands can be studied in this segment if we consider ceramic, polymeric, and metallic materials and all their variations in the structure, fundamental unit, atomic bonds, etc. For this work, the focus is directed toward the influence of copper grain size on the characteristics of ultra-short laser ablation.

The grain of a metallic material is an isolated crystal in the matter in a solid-state and its contours are chemically more reactive than its inner area [12]. Because they have a great influence on the strength, plasticity, magnetic, electrical, thermal, and optical properties of materials, the determination of the average grain size of metals is an important test in the area of materials testing and is provided for in ASTM E112-13 [13].

In this sense, the scope starts from the use of 3 pure copper samples with different grain sizes, which were metallographically prepared for an initial grain size analysis and also underwent the ultra-short laser ablation process.

In the ablation procedure itself, structures with proportionally spaced parallel lines were formed to narrow the resolution, besides varying 3 laser power levels and also 3 different repetitions in order to evaluate the material behavior when submitted both to lower ablation levels and to more aggressive processes.

The subsequent analyses of the experiment include scanning electron microscopy (SEM) to analyze the morphology and width of the ablated lines, besides the detection of thermal effects and alteration of the surface around the study target. Continuing the geometric aspects, the depth of the structures allowed by the resolution of the device was determined by a confocal laser scanning microscope (CLSM) and also in an optical microscope.

In the end, there are qualitative analyses that include burr formation, melt formation, and surface defects, and quantitative metrics that refer to structural resolution and roughness.

1.1 Motivation

Femtosecond. In a snap of fingers, approximately 1 quadrillion femtoseconds pass and you do not even notice. You do not notice because, in 1 femtosecond, the red light travels only a few hundred nanometers, which does not affect our daily life [14].

However, this scale is quite significant when it comes to atomic distances in the microcosm, where some interactions in atoms or molecules, which reflect in the physical-chemical response macroscopically, are less than the top scale of 1 picosecond [14].

Simultaneously with the advance of technology in industrial and consumer electronic devices such as mobile phones, computers, and cameras, it is noted that they would not have been possible with the maintenance of the original size of the first manufactured model. The increase in the integration of the devices with the environment must be in accordance with the practicality of its use, which is related to the decrease in size of the final product, which implies the reduction of its internal components [2].

Also used in the medical and automotive industries, the growing demand for miniaturized devices with materials other than silicon, already widely used in the manufacture of electronic microcomponents, makes the studies of laser processes increasingly attractive [2]. For presenting high resolution and flexibility to work with complex structures, laser technology is considered microtechnology that can be employed in all classes of materials with a precision lower than 10 µm, which is not possible with conventional processes [2].

Much has been studied about the influence of laser parameters in obtaining these structures, however, little is still known about the influence of material properties on the resolution and quality of the achievable structure. As there is no significant amount of studies in the area on the influence of grain size before processing, the current choice of material for high-resolution laser microstructuring is based purely on empirical phenomenological values.

The problem also extends to competing technologies such as wet chemical etching, electrical discharge machining (EDM), focused ion beam (FIB), and accelerated particles, where there are also insufficient studies on the subject. In this sense, much is lost in terms of process improvement, because, like the laser setup, the wide range of metallic, polymeric, or ceramic materials have numerous intrinsic properties that may or may not contribute to the good performance and improvement of this type of processing.

1.2 Objectives

The main objective of the work is to evaluate quantitatively and qualitatively the influence of the grain size of pure copper on the achievable structure resolution and quality during nanoscale direct ablation using ultrashort pulsed laser radiation.

In order to achieve this, some specific objectives that structure the study from the acquisition of the material used until the subsequent analyses are proposed:

- Obtaining three different grain sizes for pure copper;
- Evaluation of the feasibility of the ultrashort laser ablation process in each grain size;
- Analysis of qualitative characteristics, which include burr formation, melt formation, periodic self-assembled structures, and surface defects
- Analysis of quantitative metrics, which include structural resolution, and aspect ratio.

2 Theoretical Background

The theoretical background aims to clarify the terms and concepts already known in the literature for correlation of the executable phenomena. In this context, we first discuss the main difference in the mechanism and results when comparing ultrashort laser ablation with other scales. In the sequence, it is detailed all the ablation steps, besides the main parameters to be considered in this process.

Moving on to the materialistic area, there is the definition of grain size and the importance of its determination within the area of materials engineering, which will base the results later. In addition, the operation of the main techniques used to perform the analyses is described.

2.1 Different time scales for the laser material processing

For the efficient use of a laser in materials processing, it is necessary to understand the fundamental laws that govern the phenomena of its interaction with matter, as well as the parameters involved [15].

The advance in the technique of chirped pulse amplification (CPA) allows to evaluate the influence of the pulse duration, enabling analysis of non-stationary processes such as damage threshold and ablation [15].

In general, laser processing of materials can operate in two pulse duration regimes: long and short duration, where the latter stands out as a high quality and precision process [16].

The long duration regime occurs with the use of lasers in the nanosecond ($1ns = 10^{-9}s$) range, in which the pulse duration is longer than the thermalization time of metals. This causes the excitation to occur in the lattice. This range can be used in ablation, however, a large heat-affected zone is generated in the material [16].

On the other hand, short duration lasers comprise the durations less than 1 picosecond ($1ps = 10^{-12}s$), and ultra-short with durations less than 1 femtosecond ($1fs = 10^{-15}s$). However, from a materials processing point of view, ultrashort laser classification can be given for emissions smaller than 10 ps.The latter produces the best results in terms of well-defined spatial area with minimized thermal damage and is, therefore, suitable for the production of high-precision micromachines [16].

Figure 1 brings a comparative schematic drawing between long and short lasers at the moment of laser interaction with the solid surface. Due to the mentioned excitation difference, in the ns process, the electrons and the lattice remain in equilibrium and the solid reaches the melting temperature during the laser pulse length. Different from what occurs for the fs process, where the melting and solidification are longer, thus combining linear and non-linear absorption [1].

With this interaction difference, the linearity and consequent higher absorption and melting depth of ns processes are not applicable to the fs regime. On the other hand, the pulses have low peak powers, which leads to the agglomeration of materials by the thermal process that in turn increases the heat-affected zone. The consequent problem of the formation of this zone is the formation of defects such as cracks and chips due to redeposition and shock waves, as can be seen in Figure 1 on the left.

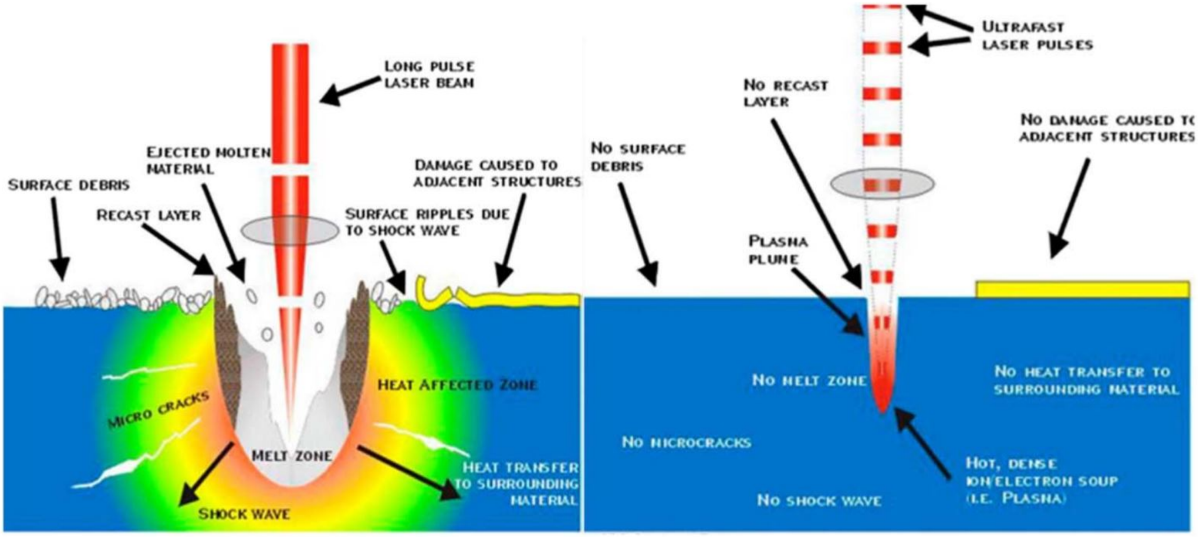

Figure 1 – Comparison of laser ablation processes with nanosecond (left) and femtosecond (right) regimes [1].

When it comes to the quality of the material ablated with a pulsed laser, the most influential parameter in this process is the pulse duration and, as mentioned, the difference of regimes leading to different interactions that consequently are explained by two physical phenomena [3].

Figure 2 brings a comparison of a real structure performed in a nanosecond (left) and picosecond (right). Even though not being in the femtosecond range, it is clear the difference in precision and quality between the regimes.

The range from ms to approximately 1 ps can be described by the classical heat conduction equation: the longer the pulse duration, the greater the thickness of the melt layer generated. With the reduction of the pulse duration and ejection of the material, the phenomenon is no longer described by the classical model, but by the two-temperature model, where the thermal behavior of the electrons and the lattice is calculated separately, which will be explained in detail later [3].

As illustrated, in the classical model, ablation comprises the processes of heat conduction, melting, evaporation, and plasma formation, since the laser energy is absorbed

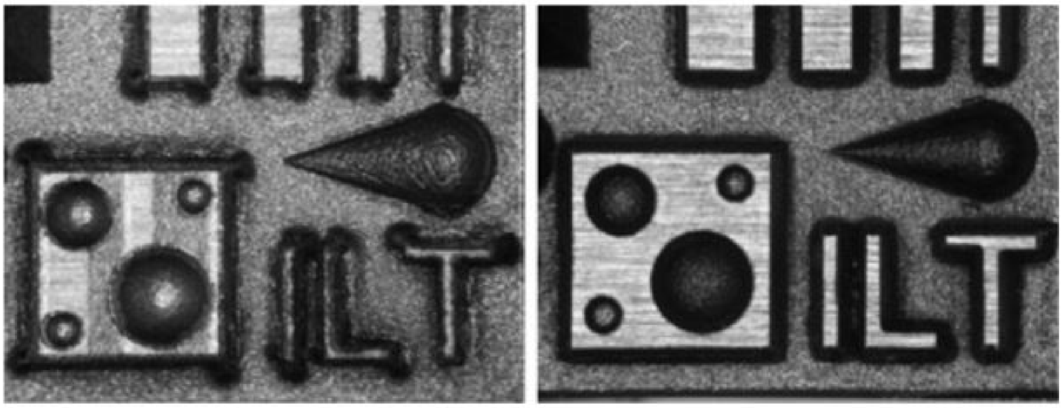

Figure 2 – Comparison between the structures formed in the laser ablation process with nanosecond (left) and picosecond (right) regimes [2]

on the surface until it forms a temperature field. In the femtosecond regime, the intensity of the pulses increases due to the absorption of multiple photons, but there is no instantaneous energy transfer [17].

For better visualization of the influence of the pulse duration on the quality of ablation, Figure 3 presents the relationship between both, where it is noted that the shorter the duration of the laser pulse the higher the quality of the structure formed, to the detriment of the lower ablation rates.

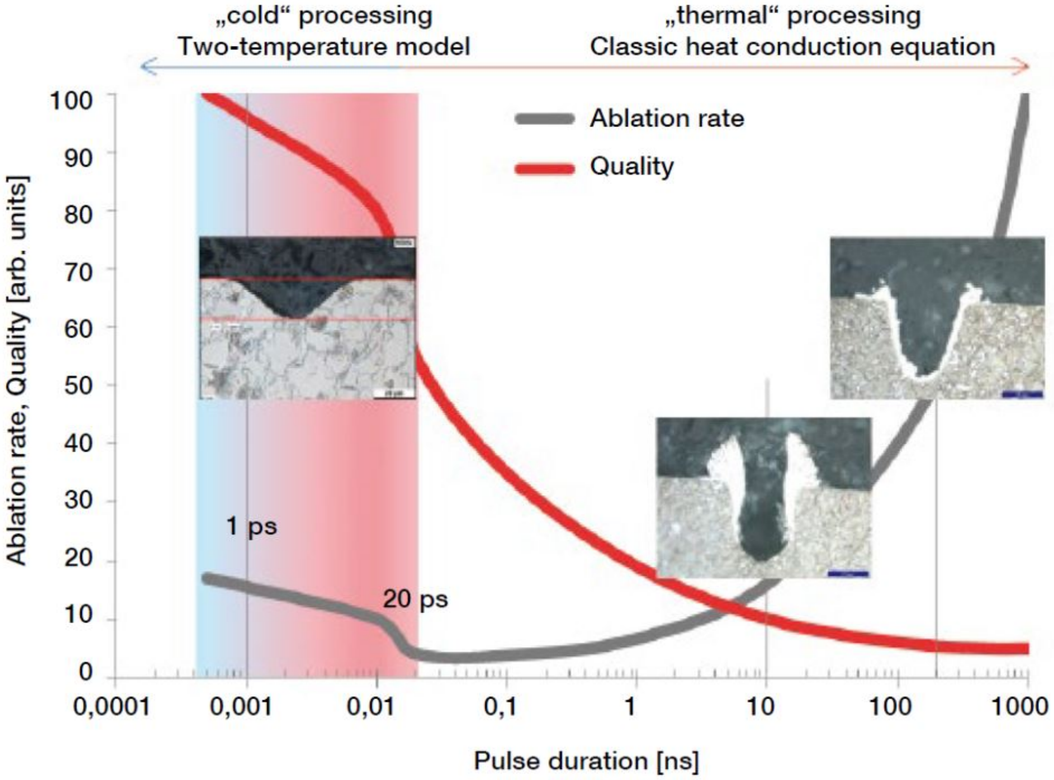

Figure 3 – Influence of laser pulse duration on the removal rate and quality [3].

2.1.1 Laser process parameters

In femtosecond laser micromachining, the laser incidence on the material is used to cause permanent micrometric damage at the surface or volumetric level. The characteristics of the structures obtained depend on the laser parameters. In order to produce complex, functional, high quality, and repeatable structures, it is necessary to control and improve these parameters during the process [18]. The main ones are: wavelength, pulse duration, pulse energy, fluence, scanning speed, spot size, repetition rate, pulse form, polarization, beam position stability and pulse-to-pulse stability [19].

Another important parameter refers to the quality of the laser beam, as well as the axial and lateral overlap during its incident operation on the material. In the axial direction, the relationship between the frequency of pulses and the speed of displacement of the laser allows the evaluation of how much, in a sequence, the next pulse covers the area reached by the previous pulse. In the lateral direction, this parameter corresponds to the adjustment of the passage of the next line of pulses, neighboring the previous line.

However, the quality of the end-product does not depend only on the adjustment of the laser parameters, but also on the combination of the properties of each material that acts as a substrate, such as thermal conductivity and reflectance. The ablation also depends on the absorption of photons, which is different for each material depending on the incident wavelength, so the absorption coefficient is also fundamental [18].

Thus, the laser parameters must be adjusted according to the result of the interaction of the material with the laser. In the end, the aim is high quality and precision of the structures, which is also a result of a low heat-affected zone with as little redeposition material as possible [18].

Figure 4 provides an overview of the properties of both the laser and the material used, as well as the parameters of the process itself. The beam radius on the workpiece is determined by the wavelength, beam quality, and focusing optics. The absorption of the radiation depends on the response of the material to a particular wavelength and also on the geometry of the surface.

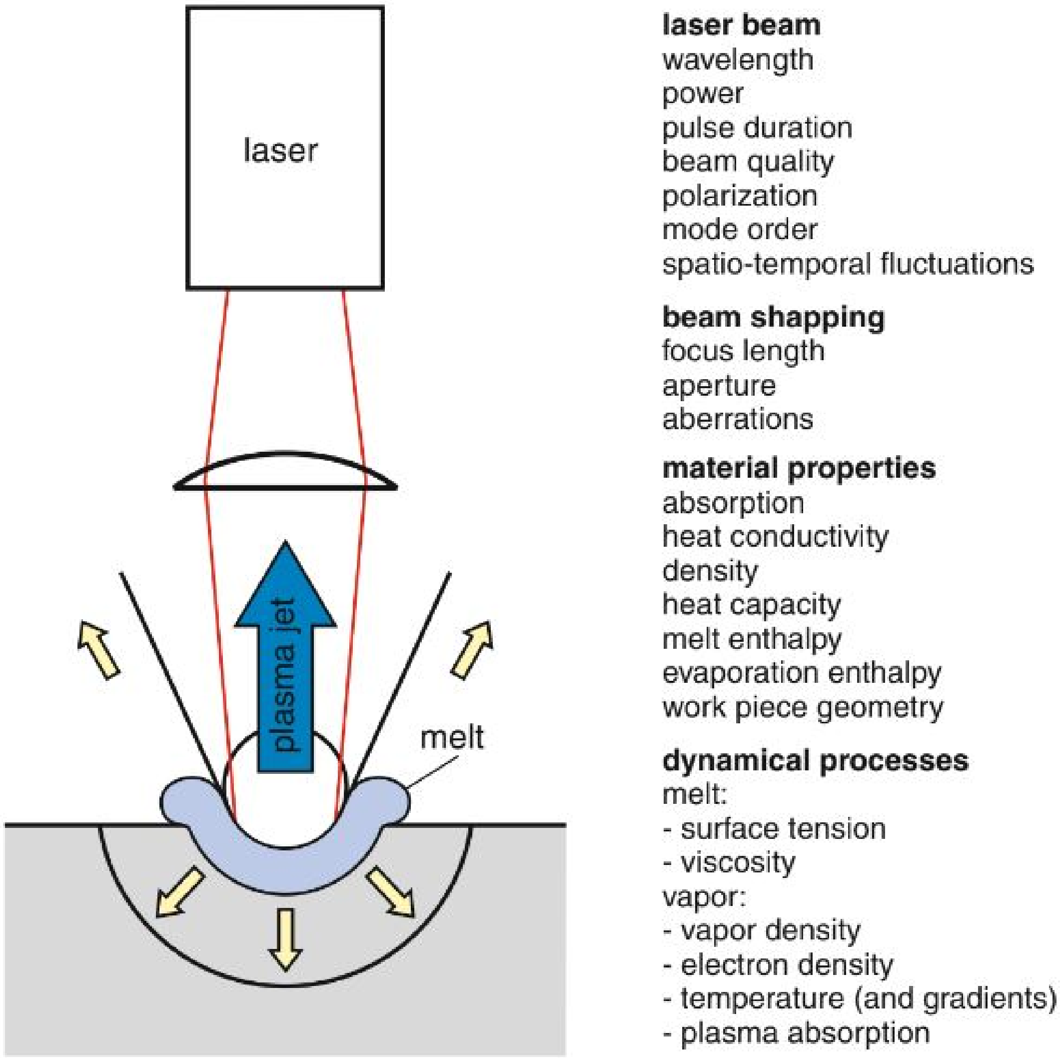

Figure 4 – Influential properties in laser processing [2].

2.1.1.1 Ablation threshold

The ablation threshold depends on the thermal and dynamic properties of the material and is dependent on the number of pulses incident on the same spot, tending to decrease with an increasing number of pulses. The ablation threshold fluence (F_{th}) is the minimum laser fluence required to start the ablation process. These definitions are important as reducing the threshold fluence can result in higher efficiency of energy coupling [20].

The ablation threshold can be determined with microscopic observations of the area in question, from which the diameter of the ablated crater (D) is plotted as a function of pulse fluence, and linear extrapolation of this plot reveals the ablation threshold [20]. Assuming a Gaussian spatial beam profile, the relationship between the crater diameter D and the maximum laser fluence F_0 can be schematized according to Figure 5 [4].

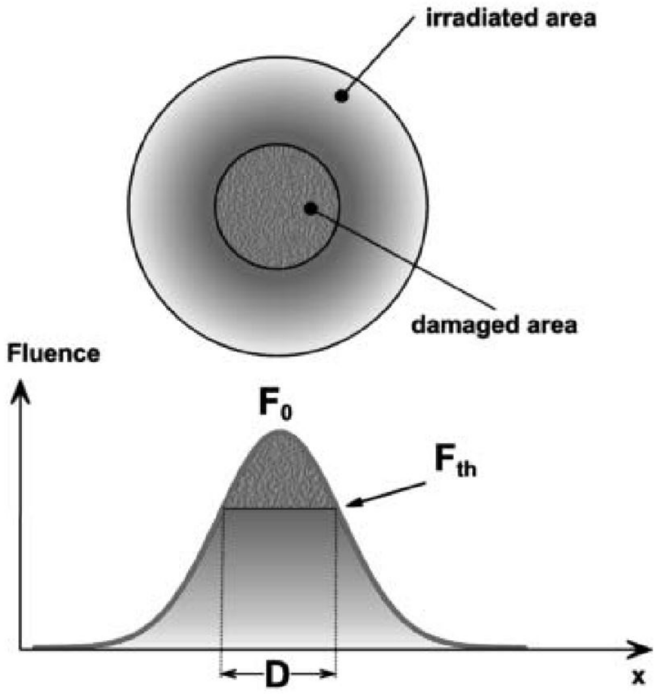

Figure 5 – Ablation topographic diagram (above) and Gaussian fluence profile (below) [4].

2.1.1.2 Crater shape

From a cross-sectional test, it is possible to calculate the final geometry of the ablated depth for both single and multiple overlapping lines, provided they have a Gaussian intensity profile and also assuming that the ablation threshold has been reached along with the entire final geometry [5].

As can be seen in the schematic Figure 6, it can be observed in a) that when the laser incurs a flat surface, the result of the ablation cavity is similar to the beam fluence profile in the focal plane. However, in subsequent incidences, the beam inclination angle is altered due to the initial modification, causing the contact surface within the formed cavity to increase [5].

Thus, as the angle tends to increase, there is a decrease in laser fluence, and consequently the ablation rate decreases. Thus, a tophat structure originated, as can be observed in b) [5].

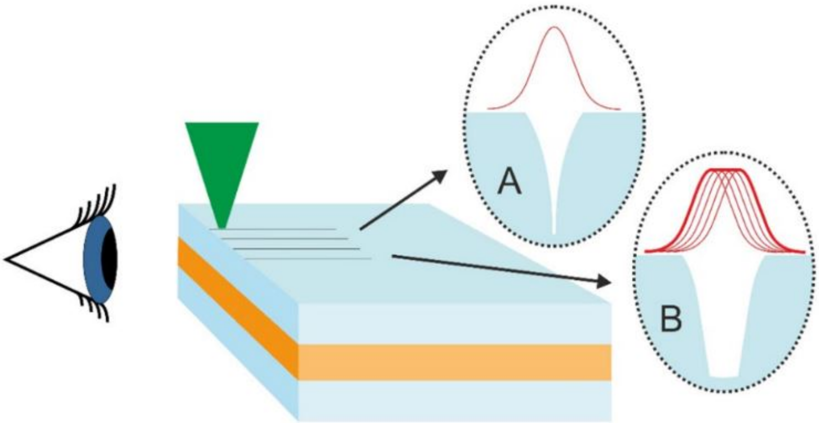

Figure 6 – Schematic drawing of a cross-section test on the sample edge with a) single lines and b) multiple lines [5].

2.2 Fundamentals of the ultrashort pulse ablation of matter

Ultrashort pulse laser ablation is a top-down technique [18] of removing material from solids using ultrashort laser pulses [7], which has its principle based on the absorption of laser energy by the material [18].

The time duration of the beam allows the sequential separation of the processes involved [7] such as melting, vaporization, and solidification of the material [21] besides presenting an excellent spatial and temporal localization of the laser-matter interaction resulting in heating and cooling rates of up to 1,000 K/ns [11]. As a consequence of this, the laser can act in a selected position without changing the rest of the properties of the part [2], limiting the zone affected by heat [22].

Although this high precision processing technique is applied to a wide range of metallic, dielectric, and semiconductor materials, the steps of the ablation mechanism using ultrafast laser pulses are different for each of the material classes [6], since metals have free electrons and dielectrics and some semiconductors have a bandgap [7].

Figure 7 shows an overview of the sequential phenomena of excitation to ablation of the mentioned materials depending on the time scale and intensity. As schematized, the first stage in yellow highlights the initial ultrafast processes [6] that occur in response to excitation in the laser pulse duration (femtosecond) [7].

In this step, semiconductors and dielectric materials can undergo non-thermal phase transformations if the excitation promotes a high concentration of free electrons. Metals, on the other hand, which absorb the laser energy more effectively, can result in plasma states or produce a Coulomb explosion with electron emission [6]. According to the abscissa axis, the intensities range from moderate ($10^{10} Wcm^2$), which induces fusion in

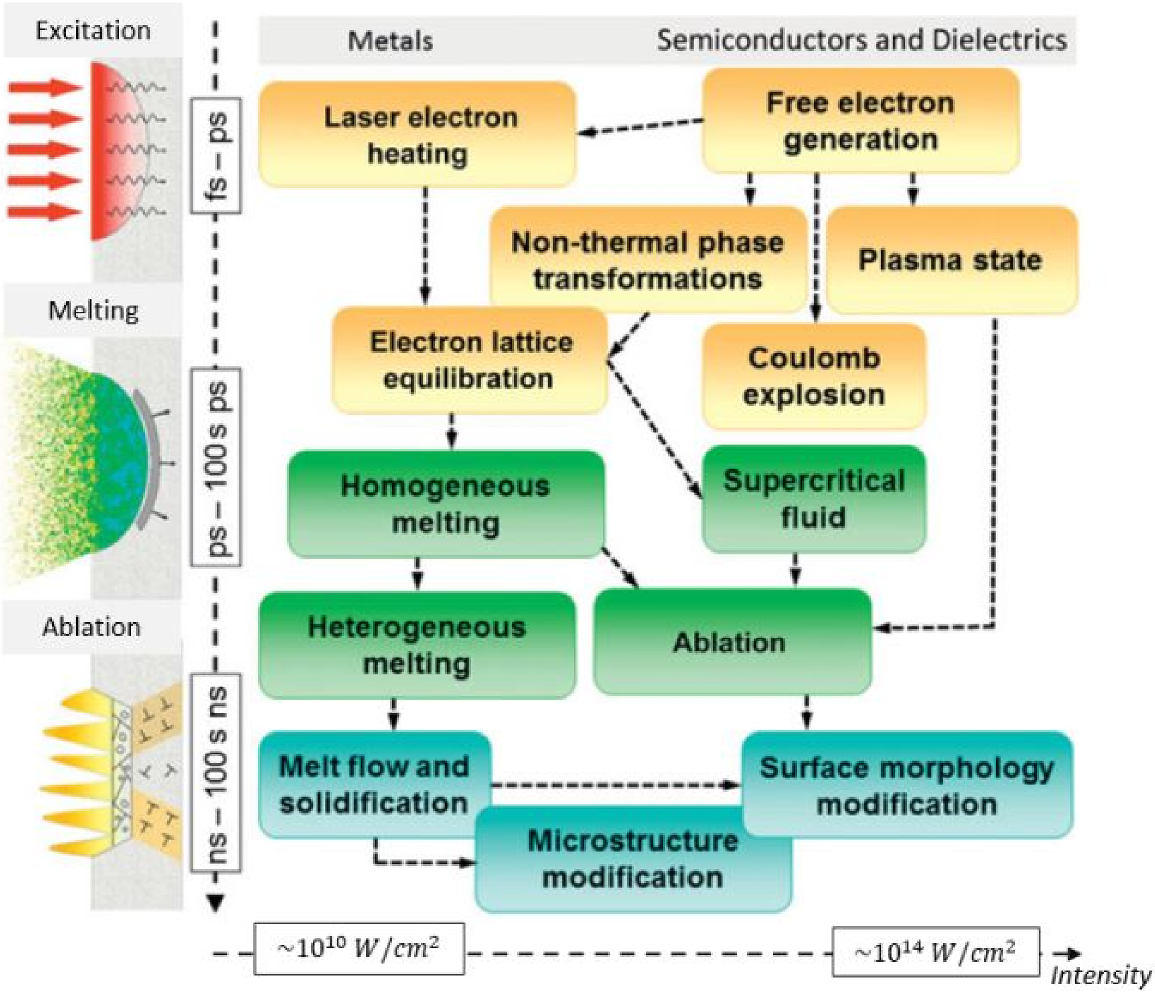

Figure 7 – Typical time scales and intensity intervals of the energy dissipation paths and phase transformations during and after the excitation of a material by an ultrashort laser pulse of about 100 fs duration [6] [7].

metals, to high ($10^{14} W cm^2$) which can drive dielectrics directly into plasma [7].

In the second step highlighted in green, melting of the material occurs which is the result of energy transfer from the electrons excited in step 1 to the atomic vibrations. This transition can entail a high melting rate and result in the inhomogeneous formation of a supercritical fluid [6]. Depending on the type of material and laser properties, the melting time is variable, but within the picosecond regime [7].

Finally, in the third stage identified with the blue color, the expansion and ablation of the laser-excited material occurs, lasting until the nanosecond regime [7] and then the cooling and solidification of the target region [6], when the temperature drops below the melting point of the material.

In the following sections, the steps of electron excitation will be further detailed, followed by melting and subsequent removal of the material [7] whose phenomena reflect in plasma formation and expansion, melting, normal vaporization, normal boiling, phase explosion, critical point phase separation and thermal diffusion and resolidification.

2.2.1 Absorption mechanisms of laser radiation

A number of photons inherent to the laser energy are incident on the material according to the Lambert-Beer law. The energy of these photons is transferred to the atoms of the material in a certain time, which is equivalent to the time of electron energy transfer to establish the temperature equilibrium. This time eq depends on the absorption properties of each material [23].

For the excitation of electrons to occur and all the phenomena that follow, the starting point is the absorption of laser light by the material in sufficient quantities for each type of mechanism. However, in some cases, the light does not have enough energy to exceed the bandgap energy of the materials, making use of non-linear processes as mentioned above [8].

Due to the band structure of each material, in metallic materials, this allows the absorption of photons with incidence energy, since the Fermi level is in the middle of an electron band [24].

However, for semiconductors and insulators, this energy is between the conduction and valence bands, so the electron must first absorb enough energy and then be raised to the conduction band, which can occur through two mechanisms: electron avalanche or multi-photon ionization (MPI) [24], which are shown schematically in Figure 8 where the valence band (VB) and the conduction band (CB) are shown [8].

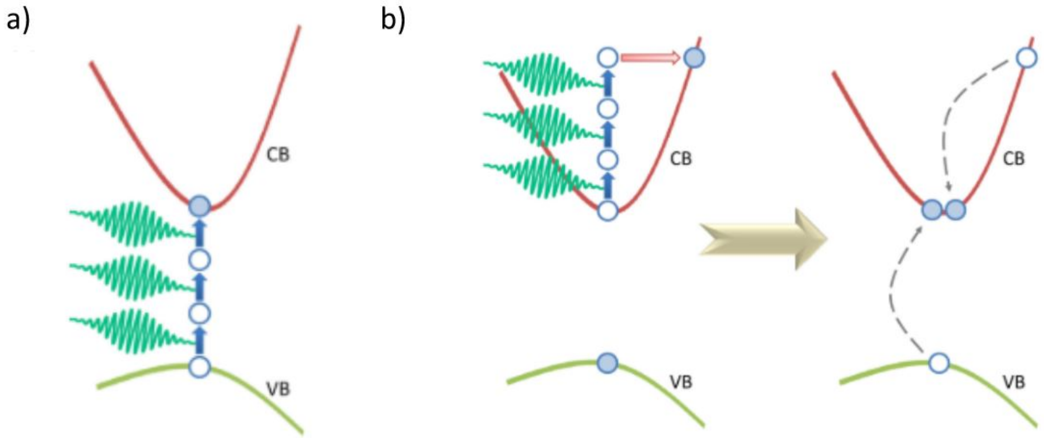

Figure 8 – Non-linear ionization absorption processes a) multi-photon (MPI) and b) avalanche [8].

The multi-photon ionization is a result of the simultaneous absorption of several photons by a single electron in the valence band, which in turn absorbs enough energy to exceed the energy of the band [8], as exemplified in Figure 8 a) where the electron needed the energy of 3 photons (in green) to move from the valence band (VB) to the conduction band (CB).

In the avalanche ionization, the same process of energy absorption of several photons occurs, however, the electron in question is already in the conduction band, exceeding the energy of the band itself. Thus, the excited electron collides with electrons of the valence band, "sharing" its energy with a new electron. This results in two electrons with lower energy but located in the conduction band. This process is repeated throughout the permanence of the laser, exponentially increasing the density of electrons in the conduction band [8].

In the case of transparent and polymeric materials, there is a non-linear mechanism of radiation absorption. This quantum problem occurs because the light frequency is lower than the range of the energy band of the material, so the probability of ionization of the atoms described in the previous processes is lower than the ionization potential itself, characterizing the nonlinear absorption mechanism [25].

2.2.2 Ablation mechanisms

As previously reported, the material response to the incidence of an ultrashort laser beam begins with a coupling of optical energy in the material, however, one cannot control the entire process based only on how the electrons are excited due to the subsequent thermal phenomena involving heat transfer, followed by the generation of a liquid-solid interface and a vapor plume [9].

The mechanism of heat conduction depends on the time scale of the laser incident on the solid, whereas for small scales the interactions take place between electron-electron and electron-phonon and are determined by the thermal conductivity of the material, characterizing the transport of electrons. For scales larger than the electron-phonon relaxation time, it is the transport of phonons that governs the conduction and redistribution of thermal energy [9].

For a better understanding of the thermal phenomena arising from the irradiation of ultrafast lasers, the next sections divide the processes into 6 main steps [9]:

- Plasma formation and electron emission;
- Non-thermal and thermal fusion;
- Normal vaporization and subsurface heating;
- Normal boiling;
- Phase separation at critical points.

2.2.2.1 Plasma formation and expansion

It is known that solid materials that have free electrons can emit them when irradiated with light beams, however, in order to have thermal conduction, the photon energy must exceed the function of the electron. The excess energy is converted into kinetic energy of the emitted electrons [9].

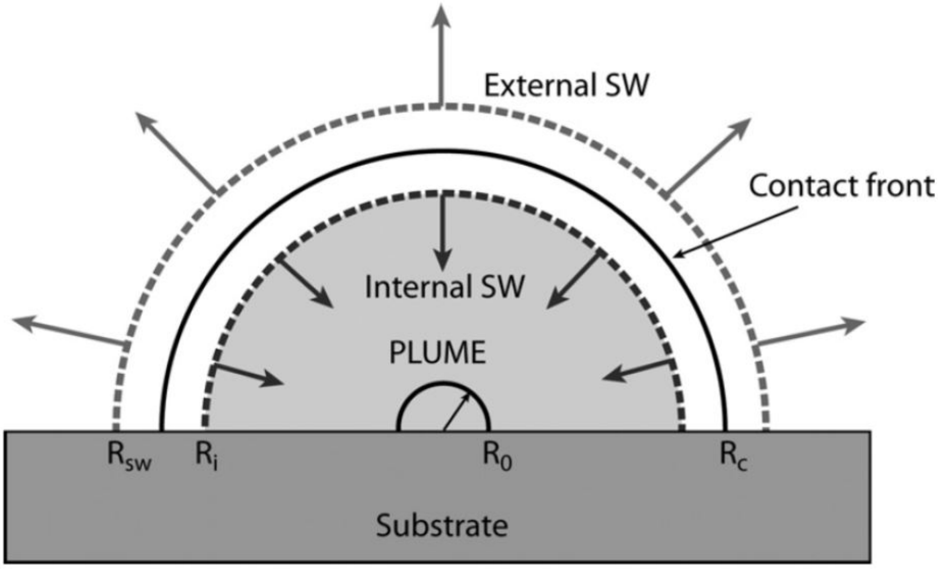

Figure 9 – Schematic model of the spherical expansion of the plume [9].

- R_0 - initial radius of the plume;
- R_c - contact front between the plume and the environment;
- R_{0c} - is moving with the speed R_{0c};
- R_{sw} - external shock wavefront;
- R_i - internal shock wave propagates inwards.

The spherical expansion model is based on the laws of conservation of mass, energy, and momentum and is conditioned on the plasma produced, which must be much smaller than the expansion distances.

Initially, as can be seen in Figure 9, the plume has a size based on the radius R_0 and has purely thermal energy (E). With the evolution of the expansion to values greater than R_0, the initial energy is transformed into kinetic energy until it reaches a maximum speed, which remains constant until the end of the expansion [9].

In a vacuum the plume can expand adiabatically, however, under atmospheric conditions considering it as a homogeneous gas, the plume acts as a piston, where the gas decelerates the plume as it is compressed and heated in the external shock wave (radius R_{sw}) if its mass is greater than that of the plume.

The temperature of the gas increases in the region of the contact front (R_c) due to a back pressure of the blade material where the molecules of the plume collide with those of the ambient gas and are reflected. The collision forms an internal shock wave (R_i) that propagates towards the interior of the system until it loses enough energy to be reflected and the plume homogenizes [9]. When the wave reaches the center, the radius R_i begins to decrease until the plume remains static and the frontal contact radius (R_c) remains constant. From that moment on, diffusion effects that are not predicted in the model must be considered [9].

2.2.2.2 Melting

The next step is the fusion of the material, which, in the femtosecond regime, are governed by macroscopic parameters such as temperature, pressure, velocity, and ablation rate because they are directly related to the atomic motion [26].

At this stage, the ultrafast laser radiation can reach temperatures above the melting temperature, however, the thermodynamic phase transitions do not happen instantaneously [9]. The material remains solid even with the heating until there is nucleation so that the liquid and/or gaseous phase expands into the solid.

This nucleation for fusion can occur in a homogeneous or heterogeneous way. Homogeneous fusion is characterized by the nucleation of the liquid phase inside the metal giving rise to several regions of liquid phase, forming a large fused region in a short time [26]. The heterogeneous fusion occurs from the surface, where there is already interfacial energy, which contributes to the nucleation energy of the liquid phase is lower, but its rate is very slow [26].

Thus, at first, the material reaches thermal equilibrium at a point slightly below the melting point, followed by heating of the central region at a temperature slightly above the melting point. This process is maintained for a sufficiently long time until the temperature of the liquid-solid interface remains constant [26].

In metallic or semiconductor materials, this nucleation starts on the surface, while for dielectrics, the nucleation begins in the volume of the material, and may be thermal or not [9].

2.2.2.3 Normal vaporization

The already known vaporization that occurs from the fused surface with the emission of particles out of the solid, which includes molecules, atoms, ions, or electrons, takes approximately 1 ns. However, this process does not remove even a single layer of atoms and does not contribute to the advancement of ablation [9].

In the vaporization that occurs laser ablation, the atoms carry heat from the surface, changing the temperature diffusion profile. In this way, the highest temperatures are below the surface, which culminates in the extraction of the material. The vaporization occurs between picosecond and nanosecond [9].

2.2.2.4 Normal boiling

Similar to vaporization, normal boiling on normal time scales involves heterogeneous nucleation within the liquid, which follows a slow process of bubble diffusion into the liquid, which cannot be accounted for in ultrashort laser ablation as a sufficiently long pulse is required [9].

2.2.2.5 Phase explosion and resolidification

Due to the fact that the boiling process in ultrashort laser ablation is homogeneous, the material quickly transits from a superheated liquid phase to a vapor phase counting a few droplets, decreasing the traction of the liquid [9]. As the temperature decreases beyond the melting point, solidification occurs in a different structure from before the laser incidence, forming a crater [9].

2.2.3 Behavior of other materials in laser ablation

Because they have different formations at the atomic and molecular level, not all classes of materials will present the same response to the same stimulus. The phenomena previously described are mostly applied to metallic and semiconductor materials, which is covered by the scope of this work. However, for other classes there are some characteristics that must be taken into consideration, as detailed in the next subsections for polymers and ceramics.

2.2.3.1 Polymers

Due to the processing time, the fragility of some polymers, and the high complexity and precision of microstructures, the use of polymeric materials in laser ablation has been advanced [27].

Unlike metals, polymers are made up of weak bonds such as van der Waals, dipole-dipole, and hydrogen bonds, and a direct comparison between them cannot be made [24]. This is due to the fact that they are represented by macromolecules, and not unitary atoms, each of which has translational and vibrational degrees of freedom [28].

Laser ablation of polymeric materials involves different processes depending on the nature of the polymer. The photothermal process involves the absorption of photons, which are released into the polymeric matrix by vibrational cooling. This mechanism causes a rapid increase in the temperature of the material, which then decomposes.

The photochemical process, on the other hand, involves the breaking of chemical bonds due to the interaction with the laser, releasing products in the form of gases. Comparatively, the latter process presents less thermal and also mechanical damage, making it possible to obtain a final structure with greater quality and precision [29].

2.2.3.2 Ceramics

Ceramics can be directly compared to metallic materials, because although they are maintained by covalent and ionic chemical bonds, these are also strong bonds, unlike polymers.

Although quite similar, the main difference between metals and ceramics in the laser ablation process is related to the Fermi energy of the electrons, that is, the energy between the valence and conduction bands.

Thus, because ceramics are insulating materials, much more energy is needed to excite the electrons and reach the conduction band. This implies the linearity of the process, where if the energy of the interval is below the energy of the incident photon, the absorption is strong and linear, otherwise, the absorption is of low intensity and non-linear nature [24].

2.3 Copper

Non-ferrous metals stand out in the mechanical, transport and especially electrical industries, where the physicochemical characteristics of their alloys are differential in engineering, being able to bring unique and irreplaceable properties depending on the application [30]. The 3 main metals for conductive applications are gold, silver and copper, the latter being the 26th most abundant element in the earth's crust [31].

Copper is a material with high thermal and electrical conductivity, with electrical resistivity equal to $1,7 \cdot 10^{-6} ohm$ and melting point corresponding to 1083 °C [30], being widely used in the electrical industry. In addition, it presents good corrosion resistance and easy machinability due to its centered face cubic structure, which, by having a dense packing of its stacked layers, causes one plane to slide easily over another [32].

The set of these characteristics makes it a promising for the manufacture of electronic components, such as conductor cables for thermal and electrical energy transmission, electrical contacts, telephony, telecommunications, automotive, civil industry, etc. [32].

2.4 Grain size

Faced with the wide range of materials available, many of them are made up of unit cells at the atomic level, whose minute structures repeat infinitely throughout the structure forming the macro material that we can observe. When materials present this repetitive atomic ordering in the three dimensions they are called crystalline materials [12].

In the case of metallic materials, these crystals are usually small, since there is a large amount of nucleus formation in the solidification process since their growth is limited when one touches the other [12]. This process can be visualised in Figure 10 where the processes of nucleation, grain growth and the appearance of the grain boundary can be observed. The microcrystal that is formed is called grain and the meeting point between them where there are different atomic combinations is called grain contour.

These grain boundaries are chemically more reactive than the internal area of the grain and can act as "barriers" to the transmission of stress or electrons, which can increase or decrease the mechanical and electrical strength of the material depending on their configuration [12].

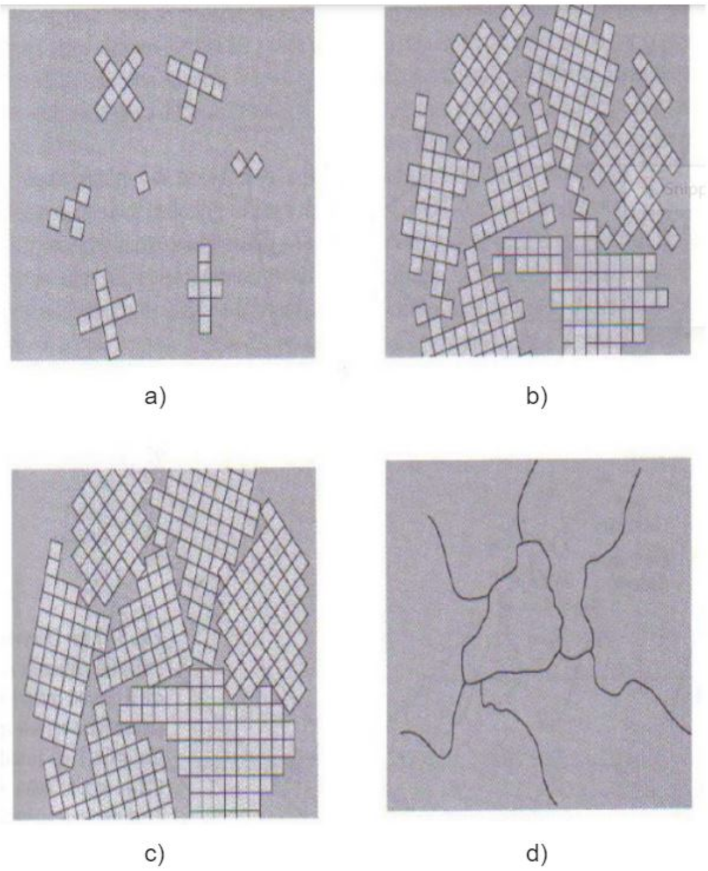

Figure 10 – Schematic of the grain formation process with a) nucleation; b) and c) grain growth and d) grain boundaries [10].

2.4.1 Grain size determination

Starting from the idea that the grain of a metallic material is an isolated crystal in the matter in a solid-state, grain size is a measure of quantitative metallography. To this end, material samples are metallographically prepared so as to make the surface flat and spectral, subsequently attacked with the indicated metallographic reagents, and evaluated in optical microscopes.

The determination of the average grain size of metals is an important test in the area of materials testing since this property directly affects the strength, plasticity [13], magnetic, electrical, thermal, and optical properties of these materials and in addition, it is a metallurgical quality control tool.

This analysis is provided for in standards such as ASTM E112-13 and ISO 643. The first original standard ASTM E112-55 Standard Test Methods for Determining Average Grain Size appeared in 1955 and since then has undergone more than 10 revisions over nearly 70 years [13]. The standard contains standard test methods for determining average grain size that can be divided into three procedures: comparison by frames, intercept, and planimetric [33].

The intercept procedure is performed by superimposing a line over the microstructure image of the material and then counting the number of intersections between these lines and the grain contours. Although time-consuming, the interception procedure is the most accurate and can minimize the statistical error with the choice of lines.

These lines can be a set of parallel vertical, horizontal or diagonal lines of the same length, as well as lines of random length and distribution and even concentric lines. The use of circles also avoids the effect of preferential grain orientation [33].

The ASTM grain size (G) is a standard value that comes from converting the grain size into microns with the following equation: $G = -3,2877 - [6,6439 \times log(L_{mm})]$, where L_{mm} is the measured grain size in millimeters. On the logarithmic scale, the higher the value of G, the smaller the grain size, as can be seen in Figure 11.

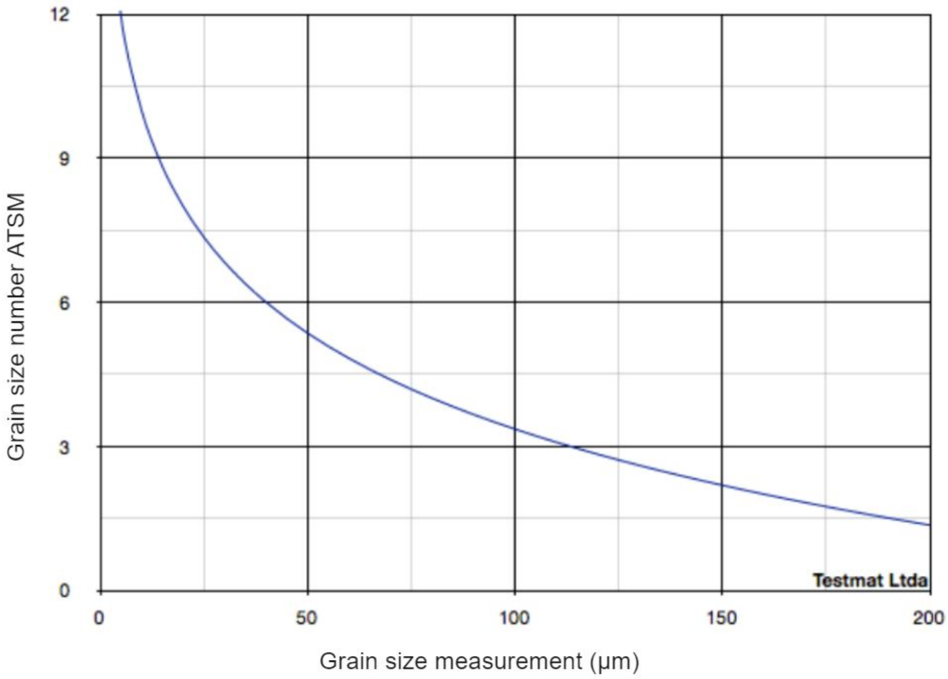

Figure 11 – Graph representing ASTM grain size number as a function of the average grain size in µm.

2.5 Analytical tools

The analysis tools are defined according to the property to be evaluated. The equipment has its limitations, so it is always interesting that the analyses are complementary so that they corroborate with the final result. In this section we will present three microscopy techniques that can analyse the same region of the sample but that will bring different points of view.

2.5.1 Optical microscopy

The first inspection of materials in an optical microscope is considered the beginning of metallurgical science and also the field of materials science. This type of equipment can be used in the microstructural analysis of various materials, which allows the analysis of phases, grain sizes, or the presence of defects [10].

Its operation is based on basic optical and illumination systems and is used for the analysis of materials opaque to visible light, such as metallic materials, where the contrasts in the image obtained are the result of different reflections in the microstructure [12].

For this, the surface of the material must have a smooth, flat, and mirror-like appearance and therefore must go through sanding and polishing steps. In addition, the microstructure must be revealed using a chemical reagent. As the region of the grain boundary in a polycrystalline sample has greater reactivity, the atoms dissolve at a faster rate than those of its former, forming grooves that are identified due to the difference in the angle of reflection [12].

2.5.2 Scanning electron microscopy

Optical microscopes although very efficient have a resolution limit of up to 2000 times depending on the diffraction response of the material when viewed with a certain light that is in the order of visible or ultraviolet light [34].

In order to increase this resolution, shorter wavelengths than the previous ones can be used, but a higher magnification requires a smaller depth of field so the sample needs to be perfectly polished [35].

In this context, the scanning electron microscope appears, where photons are replaced by an electron beam, increasing enormously the power of resolution, which can reach 300,000 times or more, as well as having a great depth of field [34].

In this way, it becomes an important instrument in the analysis of structural characteristics of solid objects, because it preserves the depth of the structure in observation and still emits images with a three-dimensional appearance necessary for the analysis of very small morphologies [34].

2.5.3 Confocal laser scanning microscopy

Confocal laser scanning microscopy (CLSM) is a technique used for recognition and construction of three-dimensional (3D) images [36], presenting advantage over a conventional optical microscope.

Its operation offers better resolution and no focus interference [36], since it rejects light that does not come from the focal plane, being possible to perform an optical cut [37]. As a result, it is possible to analyze structures within a volume of material, presenting high axial resolution and clear image quality, from which structural quantitative aspects can be analyzed [37].

3 Materials and methods

This section comprises from obtaining the copper, preparation of the samples for analysis and also for ablation, to the procedure itself and its subsequent analyses. In addition, it also brings the raw data of the measurements performed. The detailed description is of utmost importance for reproductions and improvements from this work, as well as can serve as justification in case there are questionable results.

3.1 Sample preparation

The preparation of the samples is carried out both for analyses before and after ablation and for the experiment itself, as both require the same surface characteristics. This section discusses from the receiving state of the copper, which goes through cutting, inlaying, grinding and polishing.

3.1.1 Copper delivery status

In order to obtain copper samples with quite significant grain size differences in addition to the copper in the original state, two different cooling rates were used starting from 99.9995% pure molten copper. These bulks were supplied by the Gießerei-Institut (GI) or Foundry Institute belonging to the University of Aachen Rheinisch-Westfälische Technische Hochschule (RWTH).

Figure 12 and Figure 13 show the delivery status of the copper that will later be prepared for the experiment. In Figure 12 is a bulk 40 x 40 mm wide by 3 mm thick, which has not undergone any heat treatment and will now be referred to as the small grain size (1S) sample.

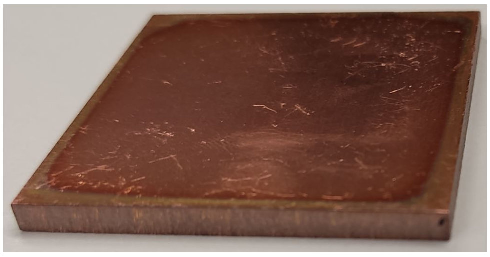

Figure 12 – Copper bulk from small grain size samples (1S).

Figure 13 shows the two solids with approximate dimensions of 80 mm in diameter and 15 mm thick that were melted at a constant temperature of 1250 °C. The solid in Figure 13 - a) underwent medium cooling, where the melt was poured into an insulated coated steel crucible at 600 °C. This sample will be called medium grain size (2M). The solid in Figure 13 - b) were subjected to slow cooling in a sand mold and is now called the big grain size sample (3B).

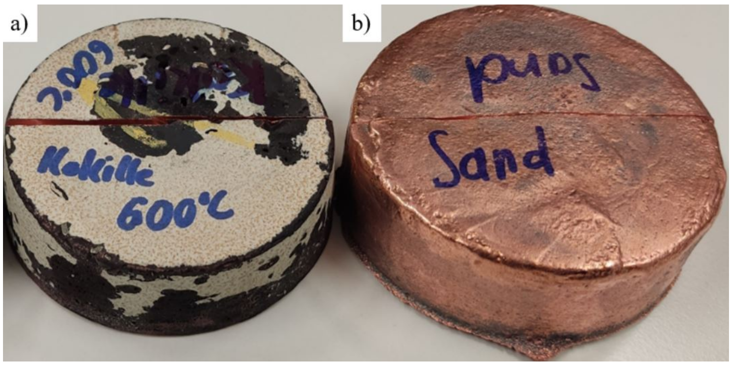

Figure 13 – Copper solids giving rise to the a) medium (2M) and b) big (3B) grain size samples.

3.1.2 Cutting and mounting

Due to the casting process is not completely controlled in terms of atmospheric gases which are trapped in the molten material, especially in sand molds, and the cooling in the mold is not homogeneous, a previous general analysis of the interior of the solids was made in order to select a homogeneous sample and with the least possible interference of pores. This way, the solid was divided into 3 parts of interest surfaces: top (T), middle (M), and bottom (B), as indicated in red in Figure 14 below. As a result of this analysis, the bottom part of the 2M sample and the middle part of the 3B sample was chosen.

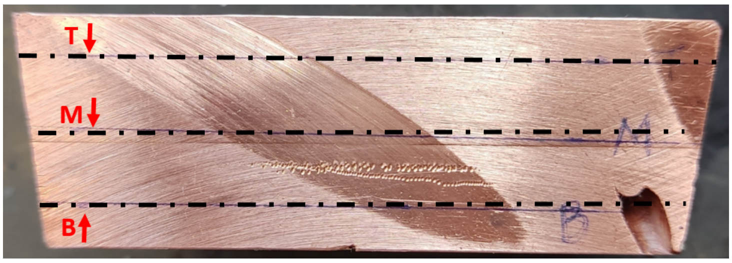

Figure 14 – Top (T), middle (M) and bottom (B) parts of interest to verify homogeneity and presence of pores of the samples from the casting.

Following the process and using a Brillant 230 wet abrasive cut-off machine, the final cuts for mounting resulted in rectangular specimens with widths of less than 100 mm and thicknesses of up to 40 mm which were subsequently mounted on an Opal 460 hot mounting press with Bakelite coating.

3.1.3 Grinding and polishing

To guarantee a sufficiently flat and polished surface both for the grain size determination via optical microscopy as well as for the ultrashort laser ablation process, after cutting and mounting the samples went through several grinding and polishing steps on a Saphir 550 Grinding and Polishing Machine.

The grinding started with 80 mesh, followed by 220, 500, 1200, 2500, and finally 4000 mesh. For the final polishing a diamond suspension (alcohol-based) mono 1 µm was used which was deposited every 3 minutes and also a lubricant dissolved in alcohol every 0,6 seconds, whose machine parameters are set specifically for copper. The steps were performed with different duration times, applied force, and rotations, as reported in Table 1.

Table 1 – Polishing and grinding parameters.

Sandpaper	**Duration**	**Force**	**Base rotation**	**Specimens rotation**
80# 220# 500#	1:30 min	150 N	300 rpm	150 rpm
1200# 2500# 4000#	1:00 min	100 N		
Polishing	15 min	15 N	200 rpm	120 rpm

3.1.4 Grain size determination

Although the metallographic preparation of mounting, grinding and polishing is the same for both optical microscopy and laser ablation process, to reveal the microstructure of the metallic materials it is necessary to perform a chemical attack.

For this, one by one the samples were submerged in a solution called "Adler" containing 25 mL of distilled water, 50 mL of 32% hydrochloric acid (HCl), 15 g of iron III chloride ($FeCl_3$), and 3 g of diammonium tetrachlorochlorocuprate (II) ($(NH_4)_2CuCl_4$), for 10 seconds.

Before any measurement, a general scan was performed on the 4 available cuts for each of the samples for selection of the best grain size homogeneity and the smallest amount of pores. Figure 15 shows the selected cuts in red for samples 1S, 2M, and 3B.

With the aid of an Olympus BX53M Optical Microscope and the Stream Motion Software, to perform the grain size determination the ASTM E 112 rule was followed. First, a macro image of the entire cut section was obtained and then a cutout of the part of interest. Then, circles and lines were drawn as specified in the method and are schematically represented in Figure 16, and then measurement points were manually added at each intersection of a grain contour with the red lines.

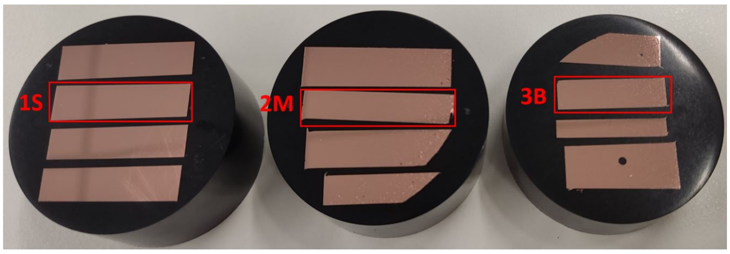

Figure 15 – Most homogeneous cuts selected for ablation for each of the samples.

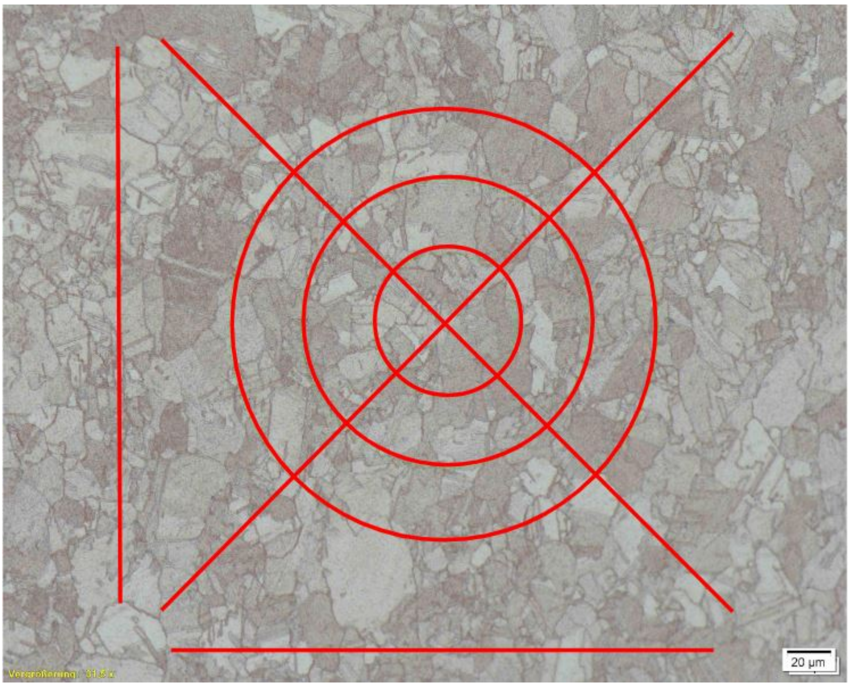

Figure 16 – Schematic of the method of grain size measurement.

3.2 Experimental setup for ultrashort laser ablation

Starting from three samples with different grain sizes, the aim is to analyze the respective behaviors of the surface and the cross section of the material when subjected to different powers and repetitions using ultrashort laser pulsed (USLP).

For this, the samples used for grain size determination were cut in half in order to create the cross section so that the ablation line could start in the sample and end at the edge, facilitating further analysis. The samples ready for the ablation process can be visualized in Figure 17 below.

Figure 17 – Cut and polished samples ready for the ultra-short laser ablation process.

The ultrashort laser ablation was performed on an FX200-1-GF with Yb:YAG device from Edgewave which consists of a laser output, a power supply and a cooler. Coupled to the laser is also a SHG-Module for FX and a THG-Module for FX, where the latter was used.

The laser scanner is located in a room at room atmosphere and temperature but with plastic curtains and ventilation to prevent dust from interfering. In addition, there is an incident exhaust fan at the ablation site so that the material removed from the sample is sucked away and not redeposited.

To define the parameters, starting at a power of 28%, whose value is close to the ideal fluence of the equipment, an increase of 3% was tried, followed by 4%. Thus, 3 different power levels were used: 28, 31 and 35%, which can be related to the power measurements, presented in Table 2 below.

Table 2 – Average power and standard deviation for each value used.

Power level [%]	**Average power [mW]**
28	5,37 ± $0,03$
31	25,34 ± $0,03$
35	113,9 ± $0,17$

As can be seen in the measurements taken at the time of the experiment for the average power at each power level, they are not directly related to each other. This characteristic is inherent to the laser device whose specification is shown in the Figure 18. As can be seen, the relationship is not linear and the lowest laser emission occurs at approximately 21%. That is, this justifies the low power for 28% power level for example. For values below 20% the emission is 0 mW.

The repetitions started with 5 times, followed by a small and a big difference, being 15 and 50 times. It is worth noting that the process used presents 75% pulse overlap, that is, 4 pulses on one line increment per repetition. In order to guarantee the reproducibility of each parameter, 3 sequential ablation lines were used with 50 µm spacing between them.

At the end of the experiment, we obtain 3 lines for each of the 3 repetitions in each of the 3 powers covered, totaling 27 ablation lines for each of the 3 samples with different grain sizes. Figure 19 shows a schematic representation of the structure formed.

Moreover, the other parameters of the process such as frequency, scanning speed, and size of the ablation as well as specifications of the equipment being the wavelength of the laser, width of the laser pulse, and magnification are specified in Table 3.

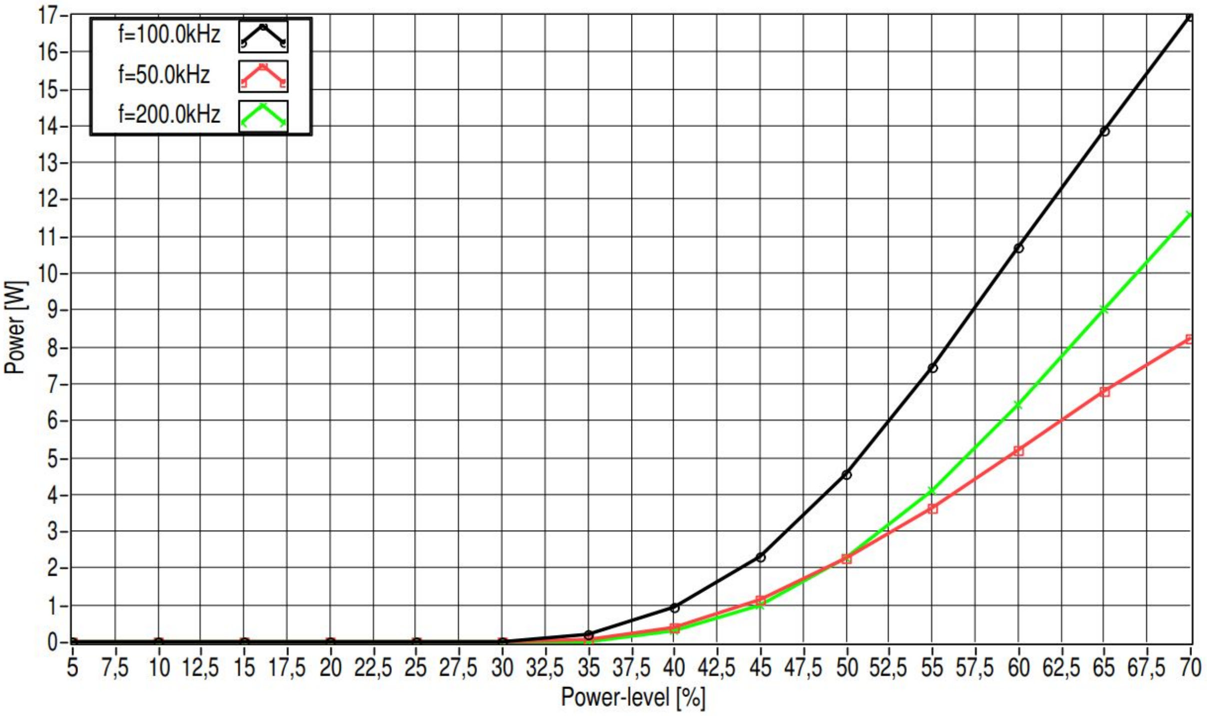

Figure 18 – Graph of power as a function of power level for the laser FX200-1-GF with Yb:YAG.

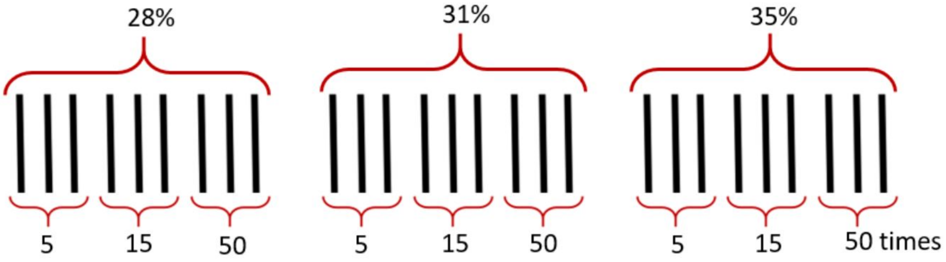

Figure 19 – Schematic representation of the structure formed by the ablation lines varying the power and repetition for each one of the samples.

Table 3 – Process parameters and equipment used in ultrashort laser ablation.

Parameter	**Value**
Frequency	100 kHz
Scanning speed	154 mm/s
Spot size	6,16 µm
Wavelength of the laser	343 nm
Pulse duration	1 ps
Magnification	3x

3.3 Analyses after ultrashort laser ablation

The analyses performed after the ultrashort laser ablation procedure comprise SEM analyses to verify the quality of the ablation and perform width measurements, CLSM analyses to verify the depth and also optical microscopy as a complement to the previous ones.

3.3.1 Scanning electron microscopy (SEM)

The scanning electron microscopy technique was used to analyse the morphology of the ablated line in the material, as well as to check the reproducibility through an overview of the structure.

For this, a Thermo Scientific Apreo 2 Scanning Electron Microscope was used and the sample was wrapped with copper tape, besides being bound with silver ink in order to guarantee the conduction of the material to the microscope base.

With the result of the images, it was also possible to measure the width of the ablation line, that is, the size of the structure formed, using the Gwyddion software. For this, the average of 5 equidistant distances along the SEM image was performed, as can be observed in Figure 20 below also in Table 4. Each measurement from M. 1 to M. 5 was performed on each ablated row represented schematically in the Figure 19 of the row for each of the samples presented in Figure 15.

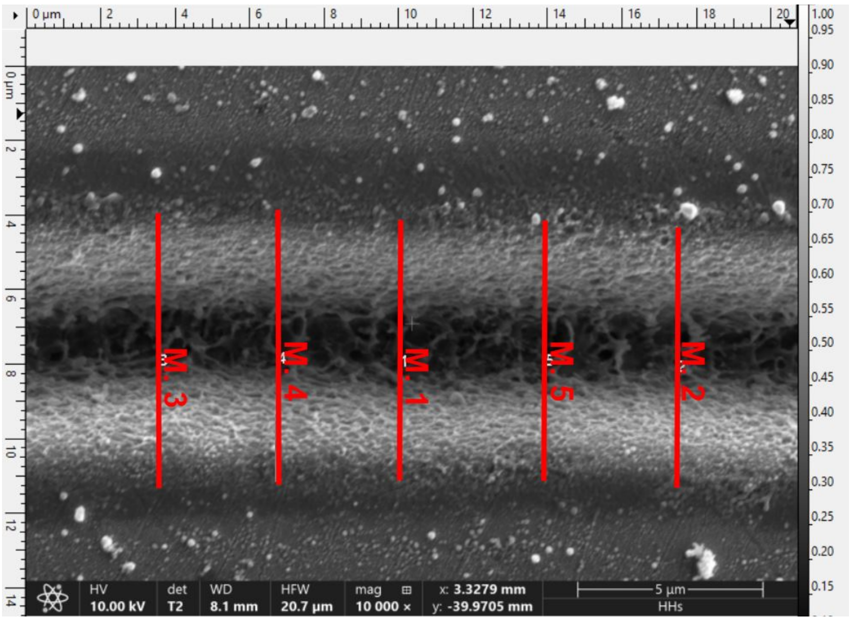

Figure 20 – Methodology for measuring the width of the ablated line using the SEM images.

Table 4 – Ablated line width measurements using SEM images.

Width [µm] ($\pm$ 0,01)								
Sample	Power level	Repetition	M. 1	M. 2	M. 3	M. 4	M. 5	Average
1S	28	5	3,91	3,86	3,32	3,51	3,64	3,64
		15	4,26	4,26	4,49	4,19	4,06	4,26
		50	7,76	7,59	8,23	7,95	8,01	7,95
	31	5	5,93	5,61	4,98	5,66	5,56	5,61
		15	8,35	8,78	9,04	9,40	9,79	9,04
		50	10,45	10,35	11,29	10,50	10,40	10,45
	35	5	7,88	7,61	7,72	7,67	7,18	7,67
		15	9,51	8,91	9,26	9,48	9,10	9,26
		50	10,74	10,38	10,44	10,53	10,50	10,50
2M	28	5	5,00	4,57	4,94	5,54	4,60	4,94
		15	5,40	5,59	5,91	5,45	5,94	5,59
		50	8,16	8,11	8,34	8,28	7,73	8,16
	31	5	6,11	6,34	6,34	6,24	5,84	6,24
		15	6,97	6,94	7,19	7,19	6,88	6,97
		50	12,52	12,32	11,81	12,29	11,93	12,29
	35	5	8,89	8,96	8,53	8,16	7,80	8,53
		15	8,88	8,75	8,61	8,43	8,82	8,75
		50	11,81	11,55	11,00	11,77	11,52	12,29
3B	28	5	5,00	5,09	5,32	5,15	4,91	5,09
		15	5,91	5,50	5,79	5,44	6,74	5,79
		50	8,02	7,41	8,22	7,78	7,61	7,78
	31	5	7,97	8,19	8,55	9,21	8,55	8,55
		15	9,02	8,50	8,88	9,19	9,05	9,02
		50	10,57	10,03	10,24	10,07	10,46	10,24
	35	5	9,49	9,05	9,87	10,18	10,99	9,87
		15	9,77	9,94	9,47	8,41	9,47	9,47
		50	9,86	9,95	10,27	9,95	10,20	9,95

3.3.2 Confocal laser scanning microscope (CLSM)

Using a Keyence VK 9710 Confocal Laser Scanning Microscope, it was possible to obtain images with colour gradients that reveal the depth of each ablated line. For visualization, the samples were first cleaned with 10% HCl solution and then subjected to analysis.

The images were then scaled using MountainMaps software, where it was also possible to visualise the profile in 3D. From these images and using the Analysis software, the depth of each structure was taken as an average of 25 measuring lines.

However, depending on the high power and repetition of the ultrashort laser ablation process, some of the lines became deeper than the detection capability of the laser microscope, and it was not possible to capture their profile and therefore they were analysed under optical microscopy which will be detailed below.

3.3.3 Optical microscopy

As mentioned earlier, the ablation lines formed from the application of 31 and 35% power with 50 repetitions were deeper than the imaging capability of the CLSM. Therefore, we started the transversal analysis of the samples with the optical microscopy to perform the measurements.

For this, the samples went through a new preparation process including embedding, grinding and polishing as detailed above, but this time focusing on cross-section analysis, Figure 21 shows the final result of the preparation.

Figure 21 – Final aspect of the metallographic preparation for optical microscopy analysis after laser ultrashort ablation.

After obtaining the images, the depth measurement was also performed with the Gwyddion software, whose methodology can be seen in Figure 22, resulting in an average of 3 measurements that correspond to the 3 equal ablation lines for each power and repetition, which are shown in Table 5.

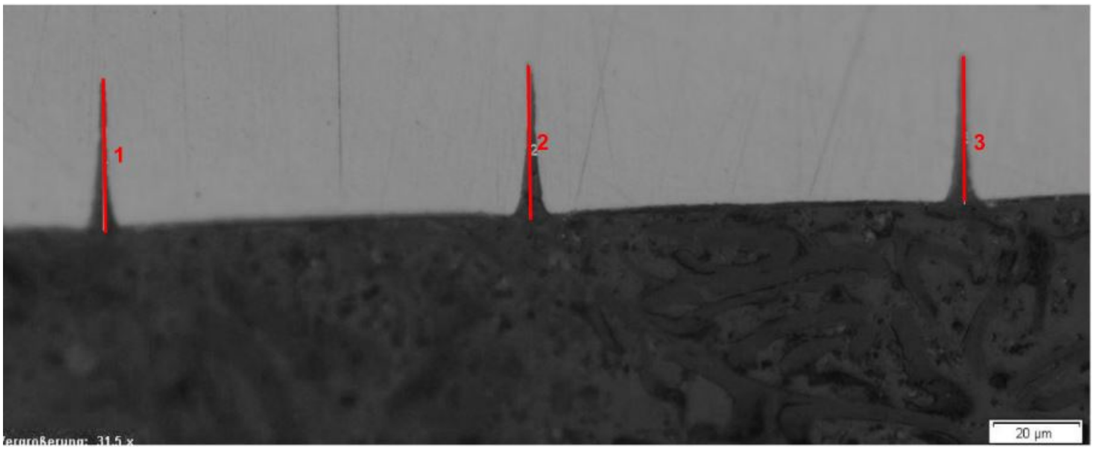

Figure 22 – Methodology for measuring the depth of the ablated line for the samples using 31 and 35% power with 50 repetitions using the optical microscopy images.

Table 5 – Ablation depth measurements for the lines with 50 repetitions.

Depth [µm] ($\pm$ 0,1)					
Sample N50	Power [%]	M. 1	M. 2	M. 3	Average
1S	31	17,9	18,5	17,9	18,1
	35	26,1	27,1	26,6	26,6
2M	31	14,7	14,7	13,7	14,4
	35	46,0	48,0	46,9	47,0
3B	31	15,2	14,2	13,7	14,4
	35	40,7	43,1	43,3	42,4

4 Results and Discussion

The results section comprises the presentation of what was measured or mapped together with a discussion based on what was presented in the background theory. Thus, there is the determination of the grain size for each sample, which governs the comparison of the study, and also the qualitative and quantitative aspects of the ablated structure.

4.1 Grain size determination

Figure 23 shows the microstructure of the entire cut of samples 1S, 2M and 3B respectively. Even without measurement and higher magnification, it is already possible to see the differences in grain size being also quite homogeneous throughout the sample.

Analyzing only Figure 23 - 2M and 3B whose solid copper came from the casting process, there is a difference both in grain size and morphology near the sides of contact with the mold, which was already expected due to the difference in cooling.

The problem is not repeated in sample 1S, which can be better visualized at a magnification of 200x in Figure 24, since it has not undergone any processing. Thus, besides being uniform, it also has no internal porosity.

As mentioned in the experimental section, the area of interest for ablation is the central part of the samples, where a cut was made in the images of Figure 25 delimited by the red dashed lines. Subsequently, the images were submitted to the determination method, and can be visualized in Figure 25 with 500x magnification, whose results are shown in Table 6.

Table 6 – Grain sizes for samples 1S, 2M and 3B.

Sample	**Grain size**	**G ATSM**
1S	10 µm	9,92
2M	525 µm	0,00
3B	1391 µm	- 4,00

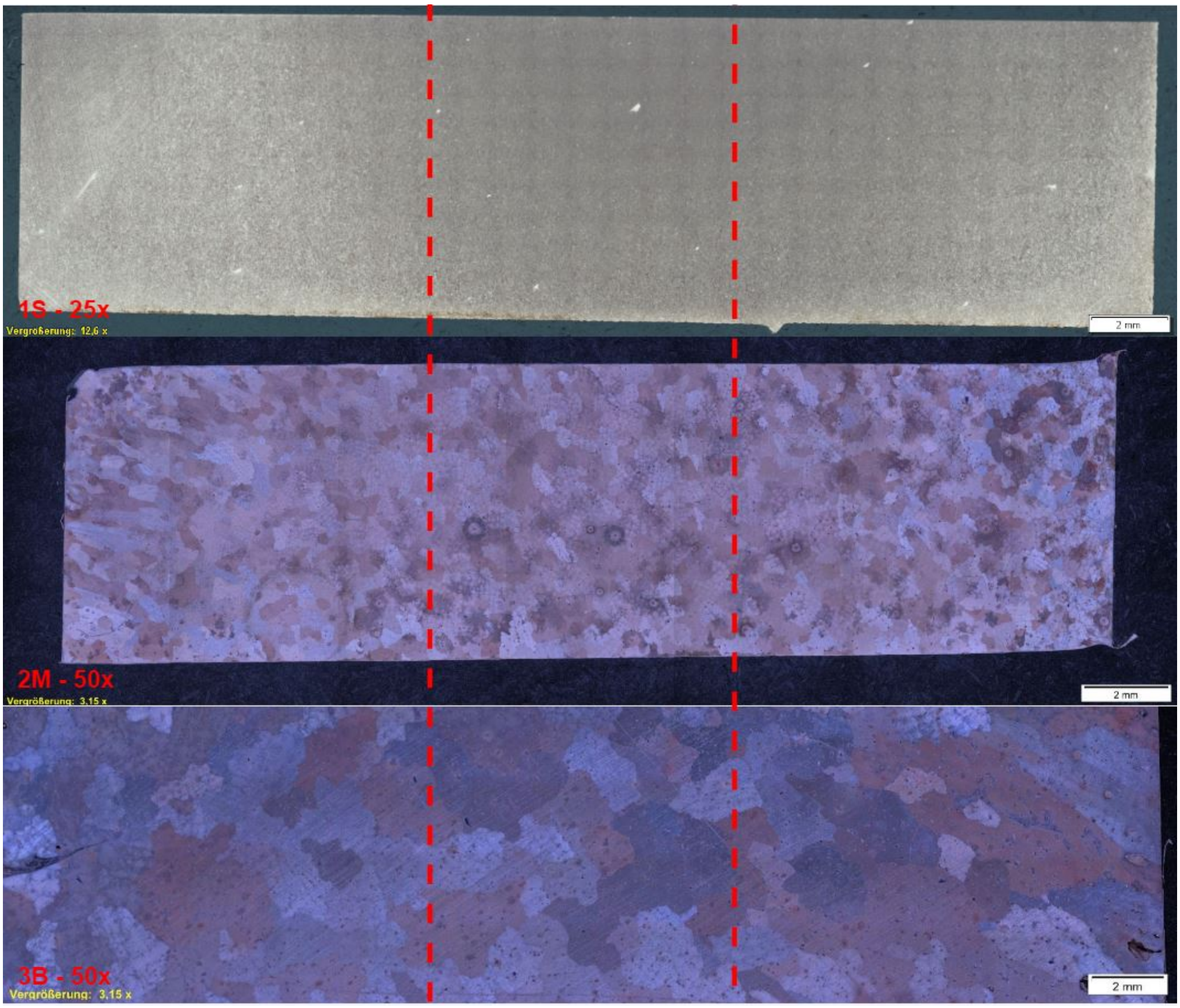

Figure 23 – Microstructure of the total cut of samples 1S at 25x, 2M and 3B at 50x magnification.

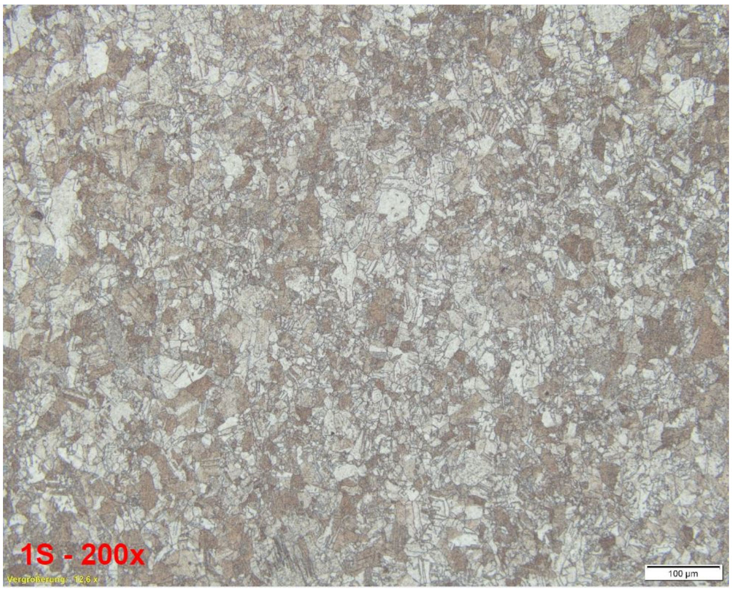

Figure 24 – Microstructure of sample 1S at 200x magnification.

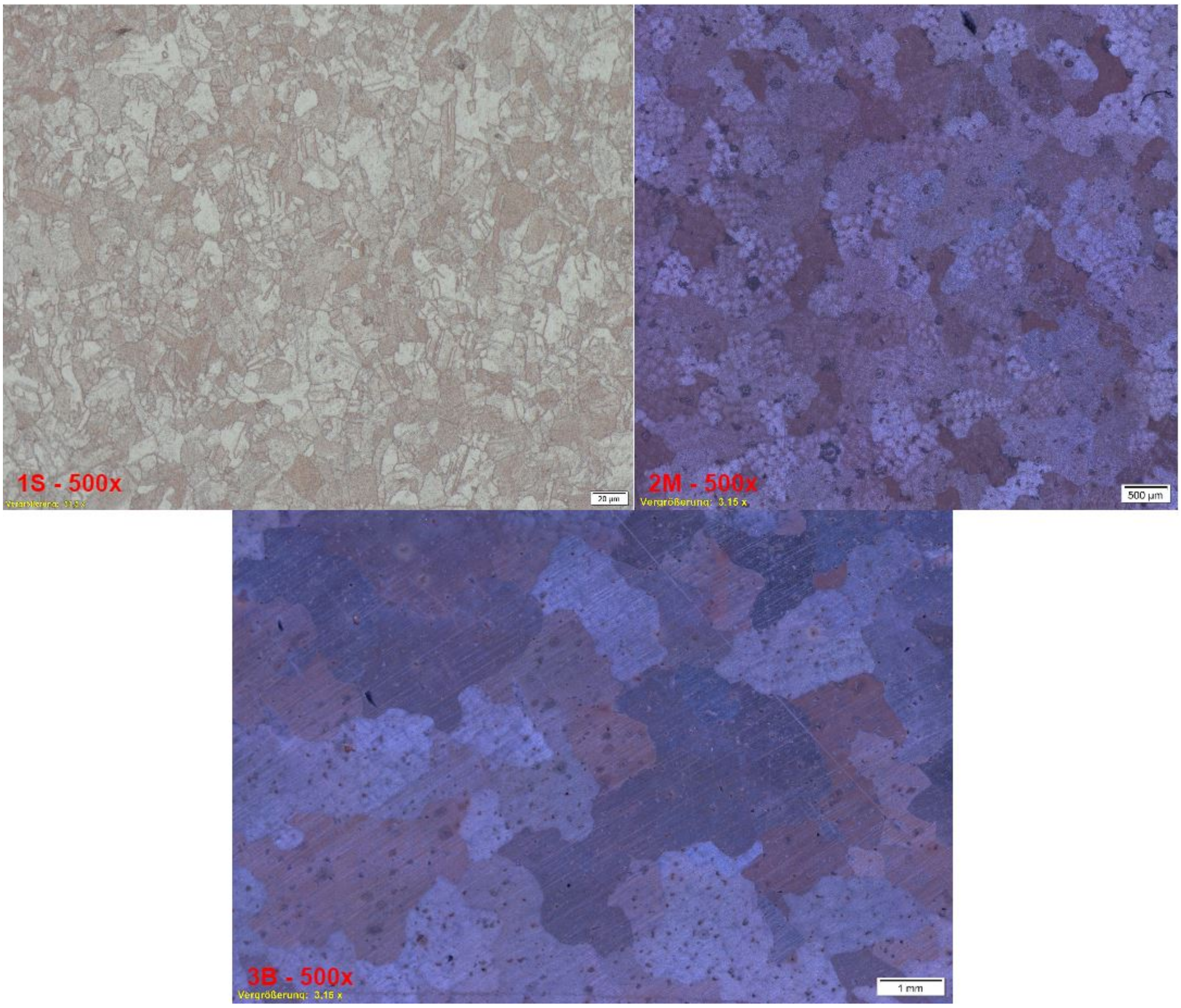

Figure 25 – Microstructure of the central region of the samples that were subjected to the grain size determination process.

4.2 Aspects of ultrashort laser ablation geometry and structure

The geometrical and structural aspects of ablation comprise qualitative results based on visual analysis of images, as will be discussed on the reproducibility and presence of ablation defects. Quantitative results, on the other hand, encompass width and depth measurements obtained through computational analyses.

4.2.1 Ablation analysis

Analysing Figure 26, one can observe an overview of the 3 ablated lines for sample 2M with power level of 35% and varying 3 repetitions. The same figure for each sample can be viewed in the Appendices 1, 2 and 3, since the result of this one extends to the others. Only one exception was made for samples 3B at 28% power level with 5 repetitions and 31% power level with 50 repetitions which had one of their ablation lines overlapped, presenting only 2 lines.

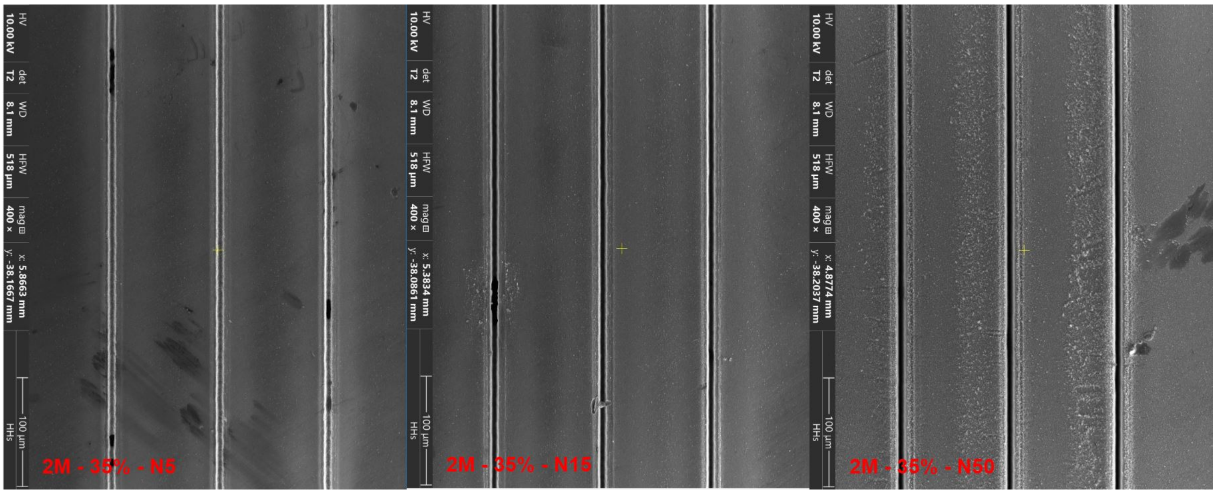

Figure 26 – SEM analysis containing an overview of all ablated lines for 35% power for 2M sample.

Analysing a section of approximately 400 µm of each line, it can be stated that in a macro vision there was reproducibility within the same process standard, since they are very similar to each other.

It is also noted that there were some small deviations especially for low repetitions. The lack of linearity at some points may be associated with the presence of pores either originating from the delivery state or may also reflect a surface unevenness due to the preparation process. However, since for high power or repetitions this deviation is minimized or non-existent, it does not significantly alter the ablation in this study.

For comparison, Figure 27 shows the copper surface with no ablation signals and Figure 28 shows a single line with higher magnification to analyze the actual ablation. Both correspond to ablation with 31% power level and 50 repetitions, however in the left Figure 28 we have the sample 1S in Figure 28 right the sample 3B. It is worth pointing out that the results are equivalent for all the samples presented in Appendices 4, 5 e 6.

From the analysis of all images it can be stated that the ablation process occurred in fact in all samples, resulting in cavities with different widths and depths depending on each parameter of variation used.

There are basically 3 regions highlighted by different shades: the grey part refers to the copper surface, the white parts would be the ablation edge and in black the cavity itself.

Both the white region along the ablation cavity and the white points observed in the copper surface region indicate material redeposition. In the region of greater concentration a puddle may have been formed and subsequent solidification, while the more distant points indicate the ejection of the ablated material, which also resolidifies.

In this aspect, the samples with different grain sizes presented quite similarity among them, with the exception of sample 3B with big grains, which appears much more ablated

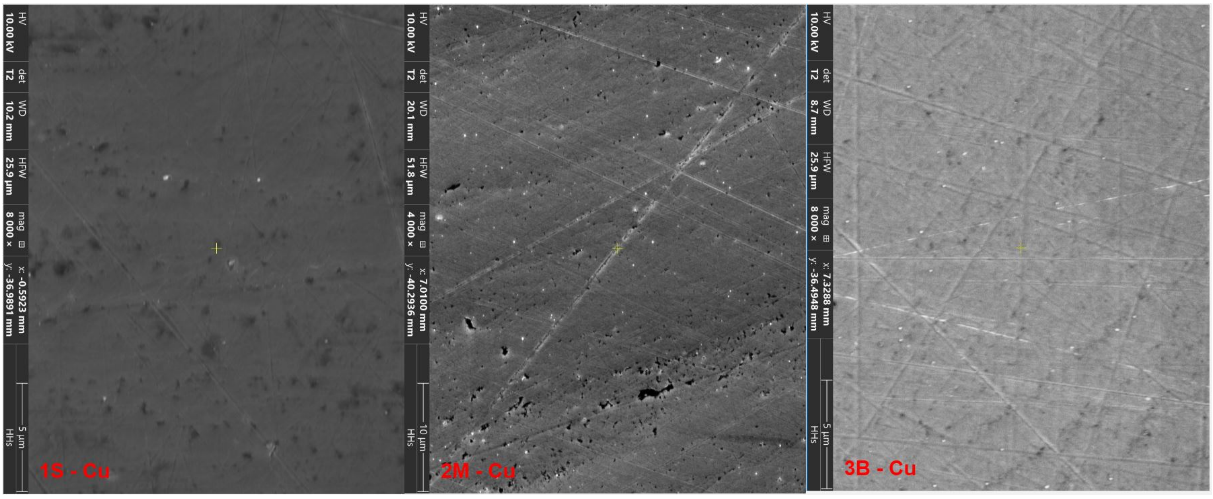

Figure 27 – Original copper surface without ablation marks of samples 1S, 2M and 3B.

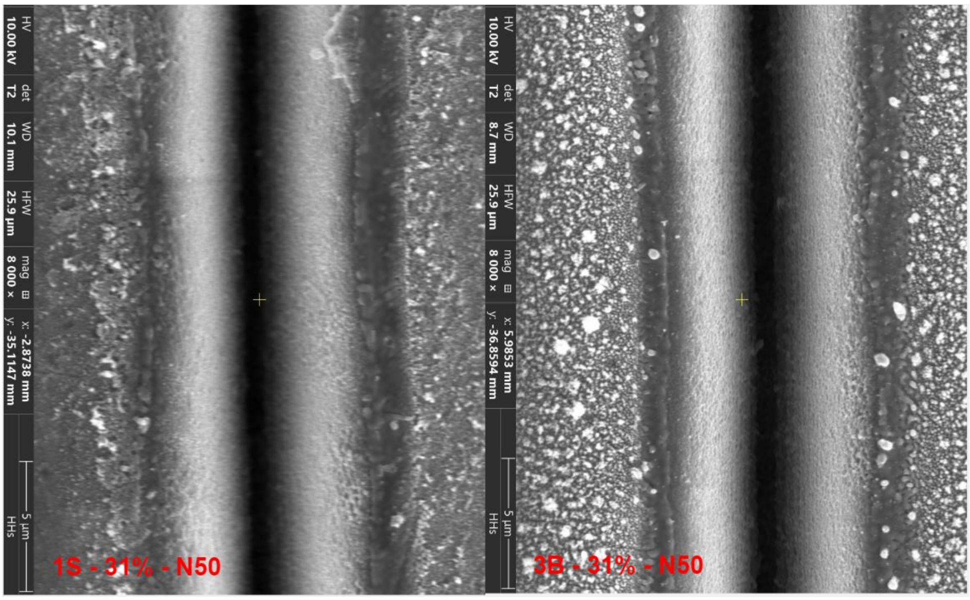

Figure 28 – Extended SEM analyses on a single ablation line for 31% power and 50 repetitions of the samples 1S and 3B.

and redeposited material mainly at higher powers, while sample 1S presents a more controlled behavior. Comparing the region around the ablated line with Figure 27, it is also noted that there was no impact on the surface at long distances.

4.2.2 Width

Analyzing the average widths in Table 7, it is noted that, as expected, lower powers with lower repetitions showed smaller ablation line width than higher powers and repetitions. It is also noted that for most lines the difference from 5 to 15 repetitions at all powers ranges between 20 and 70 µm, a pattern that is not observed from 15 to 50 repetitions.

Comparatively, samples with different grain sizes but with the same power and ablation repetition showed similar measurements. However it is important to note that all 1S measurements are slightly smaller than 2M and 3B which have less grain size variation between them. Among the latter, 2/3 of the largest widths belong to 3B, but there is no uniformity in the results.

It is assumed that the situation of the 1S measurements can be justified by the reactivity of the grain boundaries, which may act to control and dissipate energy more uniformly along the ablated structure, forming narrower cavities that minimise resolidification or ejection and redeposition of the ablated material.

Table 7 – Average ablation line width for each grain size, power and number of repetitions.

Average width [µm] ($\pm$ 0, 01)				
Power [%]	Repetition	1S	2M	3B
28	5	3,64	4,94	5,09
	15	4,26	5,59	5,79
	50	7,95	8,16	7,78
31	5	5,61	6,24	8,55
	15	9,04	6,97	9,02
	50	10,45	12,29	10,24
35	5	7,67	8,53	9,87
	15	9,26	8,75	9,47
	50	10,50	12,29	9,95

4.2.3 Depth

The Figure 29, Figure 30 and Figure 31 brings an analysis of depth by gradient staining from the images obtained by the CLSM. However, as mentioned earlier, some deeper measurements are not supported by the device and were then analysed in the optical microscope and all measurements are shown in Table 8. The images used for depth measurement under an optical microscope can be found in Appendices 7, 8 and 9.

Although we are comparing depths obtained by different methods, it is still possible to roughly infer information due to the great difference in values from one to the other. However, it is important to point out that the depths measured by CLSM present greater reliability and precision than those obtained by optical microscopy images.

Overall the data are similar and consistent for each parameter, however, unlike the width measurements, a peculiarity is noted for sample 1S, which its depth measurements are slightly larger than samples 2M and 3B which have larger grain size. Except for the exception with 35% power and 50 repetitions, which presents a significantly lower depth.

Corroborating with the previous width study, this last data can also be justified with an energy dissipation by the grain boundaries, this time in a more significant way due to the longer length and consequently higher density of the grain boundaries. Furthermore, the results agree with the previous ones in that the higher powers and repetitions present greater depth and consequently greater ablated volume.

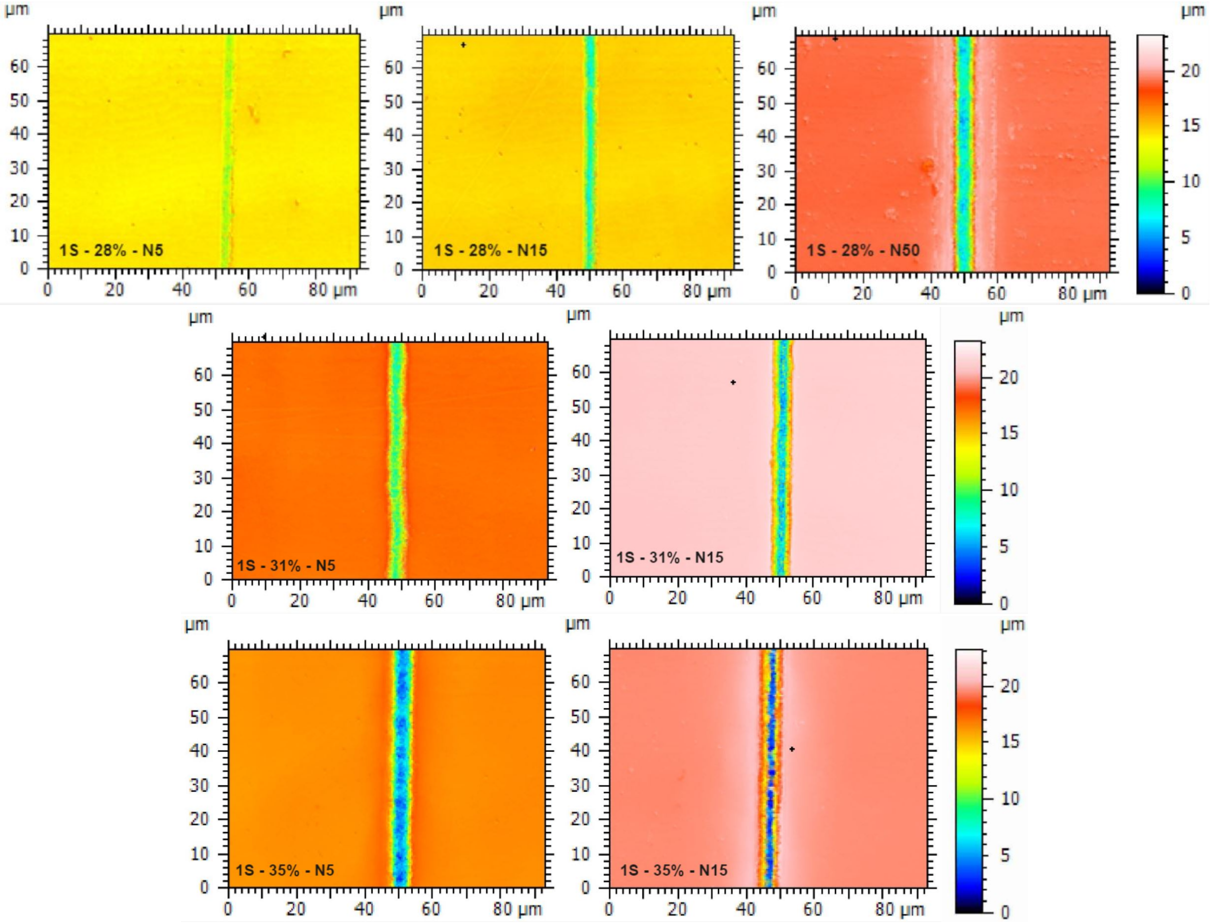

Figure 29 – Topographic representations of the ablated cavity depth for sample 1S.

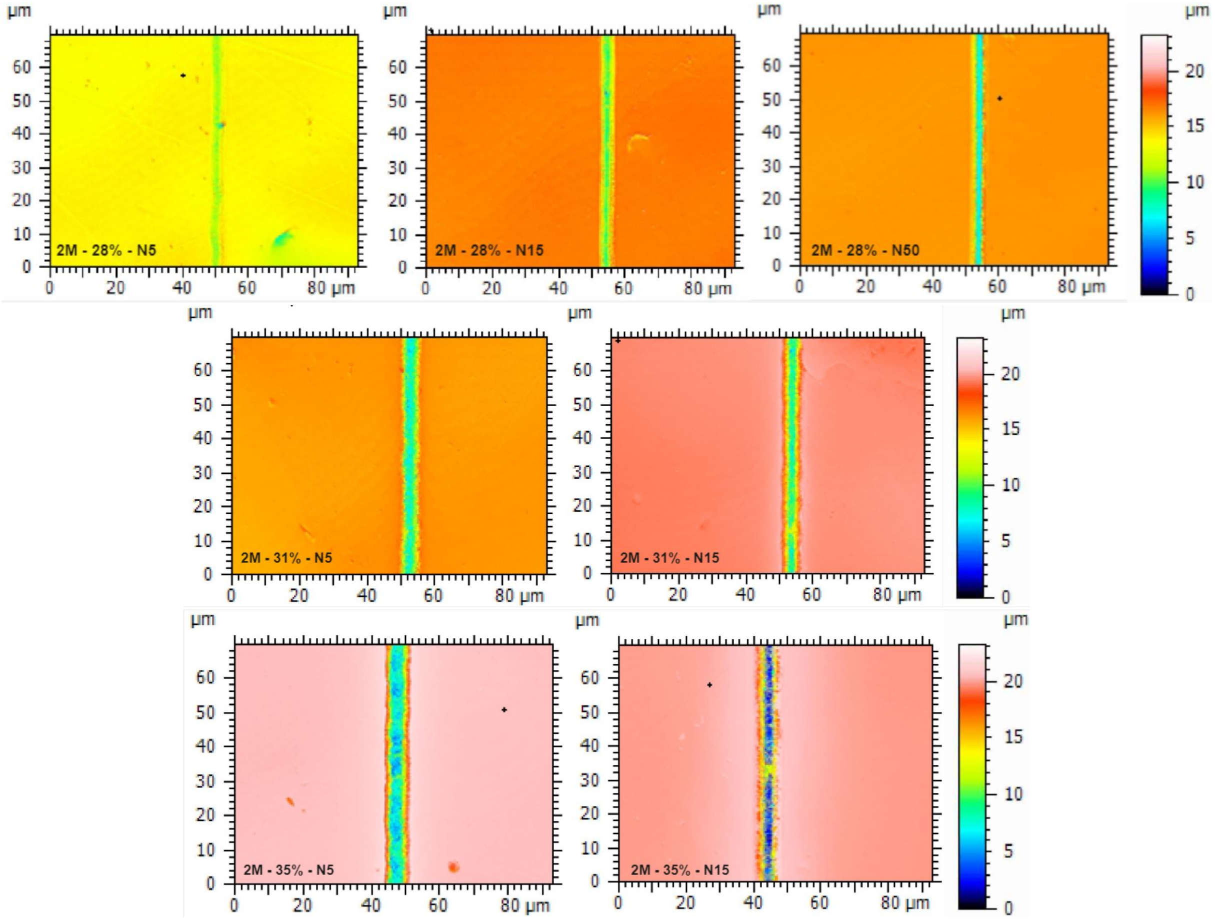

Figure 30 – Topographic representations of the ablated cavity depth for sample 2M.

Table 8 – Average ablation line depth for each grain size, power and number of repetitions.

Average depth [µm] ($\pm$ 0,01)				
Power [%]	Repetition	1S	2M	3B
28	5	0,31	0,49	0,39
	15	1,16	1,14	1,04
	50	5,17	2,99	3,62
31	5	1,19	1,95	1,70
	15	7,68	6,26	5,66
	50	18,10	14,40	14,40
35	5	5,56	7,05	5,71
	15	16,17	14,45	17,08
	50	26,60	47,00	42,40

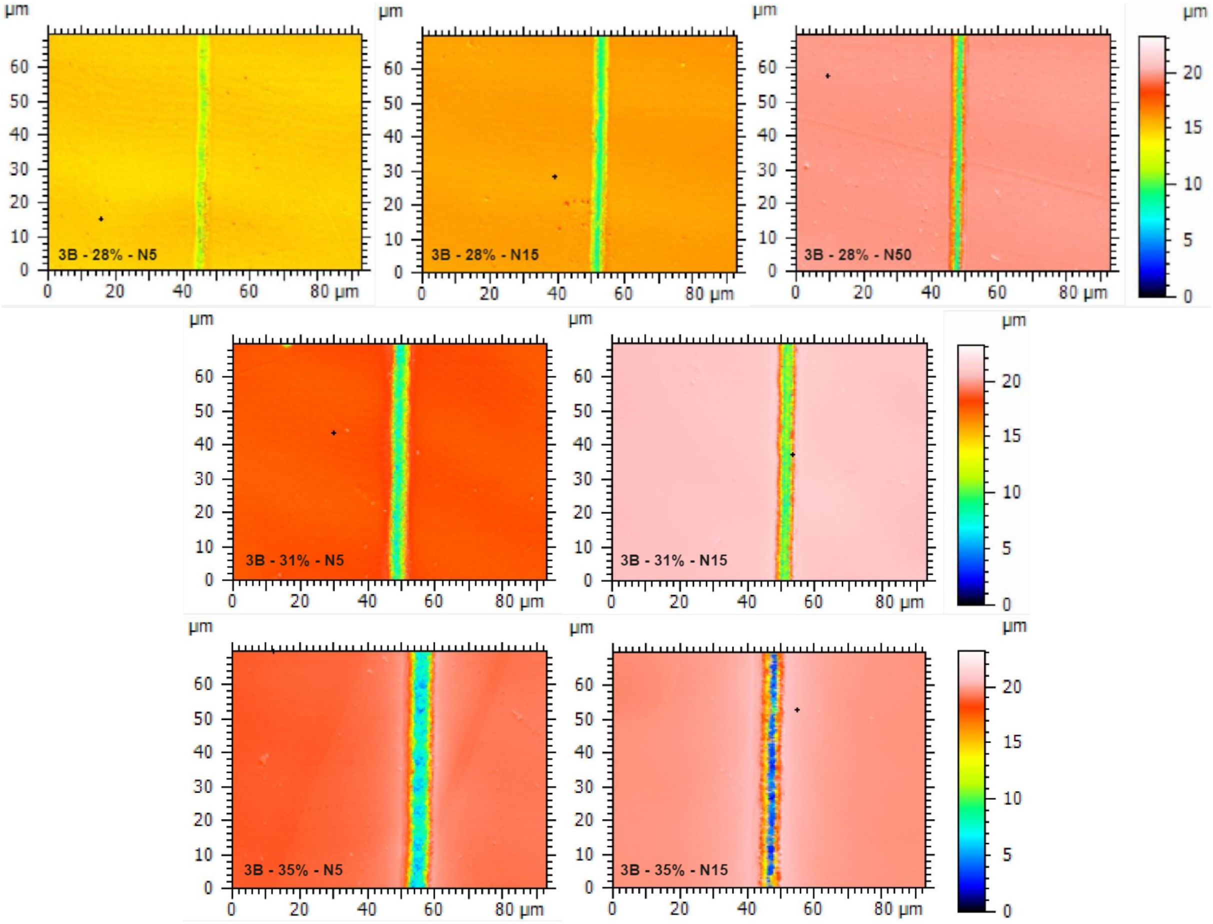

Figure 31 – Topographic representations of the ablated cavity depth for sample 3B.

5 Conclusions

In view of the aspects and analyses presented, firstly it was successful in obtaining samples with different grain sizes, as well as the complete analysis of the sample and the choice of the most homogeneous region was fundamental, giving reliability to the final result.

It can also be concluded that ultrashort laser ablation is effective for pure copper in its different grain sizes, as well as different laser processing parameters such as power level variation and the number of repetitions on the ablated line. In addition it can be stated that there is reproducibility within the same process pattern.

Analyzing the geometric characteristics of the formed structure and taking into account that the sample with the smallest grain size (1S) had the smallest average width and depth, it can be inferred that at first, the higher density of grain contours contribute to the quality of the final formed pattern because it acts in the control and dissipation of energy. This makes the process more homogeneous and consequently the structure obtained is more uniform in comparison with samples 2M and 3B with larger grain sizes that initially presented a greater amount of ablated and redeposited material.

Given the above, it can be concluded that the use of small grain sizes for the ultrashort laser ablation process gives rise to more uniform structures, with higher quality and pattern when higher ablation power level is used.

5.1 Contributions

The present study is important for the scientific community due to the importance of the subject in face of the current technological advancements. An area not much explored so far and without comparison with competitive technologies is always a great challenge.

The survey of the need for the work can start a series of studies both for the continuation of the use of copper and for other materials, besides the exploration of other properties.

The experimental methodology may become a model for future work and the results of this study may contribute to processing improvement using ultra-short laser ablation.

5.2 Future work

As a continuation of the current work, it may be interesting to verify the microstructure of the cross-section of the ablated material, since some thermal effects from the ablation process and also the behavior of the cavity profile can be identified. And yet, due to the results, it would be interesting to study monocrystalline materials.

Besides extending the study to ceramic and polymeric materials, there is also a wide range of properties for metallic materials such as grain orientation, purity, thermal conductivity, and thermal expansion that can be studied.

Some suggestions for further use of copper are the influence of the degree of purity and grain size orientation. In addition, the purity grades of nickel can be compared with nickel-phosphorus alloy and also use silver to determine the influence of thermal conduction.

References

1 PHILLIPS, K. C. et al. Ultrafast laser processing of materials: A review. *Advances in optics and photonics*, OPTICAL SOC AMER, WASHINGTON, v. 7, n. 4, p. 684–712, 2015. ISSN 1943-8206. 9, 16, 20

2 PROPAWE, R. *Tailored Light 2 : Laser application technology.* Heidelberg [u.a.: Springer, 2011. ISSN 1865-0899. ISBN 3642012361. 9, 16, 17, 21, 23, 25

3 MAYERHOFER, R.; MAY, A. B.; SERBIN, J. Is it cold enough, yet?: Considerations on the use of ultrashort-pulsed lasers for material processing. *Laser-Technik-Journal*, v. 13, n. 1, p. 20–23, 2016. ISSN 1613-7728. 9, 20, 21

4 KRÜGER, J.; KAUTEK, W. Ultrashort pulse laser interaction with dielectrics and polymers. *Polymers and Light*, Springer, p. 247–290, 2004. 9, 23, 24

5 STROJ, S.; PLANK, W.; MUENDLEIN, M. Ultrashort-pulsed laser separation of glass-silicone-glass substrates: influence of material properties and laser parameters on dicing process and cutting edge geometry. *Applied physics. A, Materials science processing*, Springer Berlin Heidelberg, Berlin/Heidelberg, v. 127, n. 1, 2020. ISSN 0947-8396. 9, 24, 25

6 SHUGAEV, M. V. et al. Fundamentals of ultrafast laser–material interaction. *MRS bulletin*, Cambridge University Press, New York, USA, v. 41, n. 12, p. 960–968, 2016. ISSN 0883-7694. 9, 16, 25, 26

7 RETHFELD, B. et al. Modelling ultrafast laser ablation. *Journal of physics. D, Applied physics*, IOP Publishing, BRISTOL, v. 50, n. 19, p. 193001, 2017. ISSN 0022-3727. 9, 16, 25, 26

8 AMS, M. et al. Investigation of ultrafast laser–photonic material interactions: Challenges for directly written glass photonics. *IEEE journal of selected topics in quantum electronics*, IEEE, PISCATAWAY, v. 14, n. 5, p. 1370–1381, 2008. ISSN 1077-260X. 9, 27, 28

9 MINGAREEV, I. *Ultrafast dynamics of melting and ablation at large laser intensities.* Göttingen: Cuvillier, 2009. 9, 28, 29, 30, 31

10 FILHO, R. P.; PANTANO, P. M. Microscopia óptica: Determinação de tamanho de grãos. *INTELLECTUS. Revista do Grupo Polis Educacional.*, p. 62. 9, 33, 35

11 STAFE, M.; MARCU, A.; PUSCAS, N. N. *Pulsed laser ablation of solids: basics, theory and applications.* [S.l.]: Springer Science & Business Media, 2013. v. 53. 16, 25

12 JUNIOR, W. D. C.; RETHWISCH, D. G. Ciência e engenharia de materiais: uma introdução. *Rio de Janeiro: LTC*, v. 589, p. 249, 2002. 16, 32, 33, 35

13 BI, G. et al. Acceptability analysis for determining the average grain size by astm e112 standard. In: IOP PUBLISHING. *IOP Conference Series: Materials Science and Engineering.* [S.l.], 2020. v. 770, n. 1, p. 012023. 16, 33, 34

14 DIELS, J.-C. et al. *Ultrashort Laser Pulse Phenomena: Fundamentals, Techniques, and Applications on a Femtosecond Time Scale*. San Diego: Elsevier Science Technology, 2006. ISBN 0122154932. 17

15 CHICHKOV, B. et al. Femtosecond, picosecond and nanosecond laser ablation of solids. *Applied physics. A, Materials science processing*, SPRINGER, NEW YORK, v. 63, n. 2, p. 109–115, 1996. ISSN 0947-8396. 19

16 HAMAD, A. H. *Effects of different laser pulse regimes (nanosecond, picosecond and femtosecond) on the ablation of materials for production of nanoparticles in liquid solution*. [S.l.]: IntechOpen London, UK, 2016. 19

17 LEITZ, K.-H. et al. Metal ablation with short and ultrashort laser pulses. *Physics procedia*, Elsevier B.V, v. 12, n. 2, p. 230–238, 2011. ISSN 1875-3892. 21

18 RAVI-KUMAR, S. et al. Laser ablation of polymers: A review. *Polymer International*, Wiley Online Library, v. 68, n. 8, p. 1391–1401, 2019. 22, 25

19 HE, C. *High-precision and Complex Geometry Helical Drilling by Adapted Energy Deposition
Hochpräzisions-Wendelbohren komplexer Geometrien mittels angepasster Energiedeposition*. Aachen: Apprimus Verlag, 2020. 22

20 NATHALA, C. S. R. et al. Ultrashort laser pulse ablation of copper, silicon and gelatin: effect of the pulse duration on the ablation thresholds and the incubation coefficients. *Applied physics. A, Materials science processing*, Springer Berlin Heidelberg, Berlin/Heidelberg, v. 122, n. 2, p. 1–8, 2016. ISSN 0947-8396. 23

21 MIN, J. et al. Application of laser ablation in adhesive bonding of metallic materials: A review. *Optics and laser technology*, Elsevier Ltd, v. 128, p. 106188, 2020. ISSN 0030-3992. 25

22 HODGSON, N. et al. Ultrafast laser machining: process optimization and applications. In: *Proceedings of SPIE - The International Society for Optical Engineering*. [S.l.]: SPIE, 2021. v. 11673, p. 1167308–1167308–21. ISBN 9781510641815. ISSN 0277-786X. 25

23 NEDIALKOV, N. et al. Dynamics of the ejected material in ultra-short laser ablation of metals. Springer Berlin Heidelberg, Berlin/Heidelberg, v. 79, n. 4, p. 1121–1125, 2004. ISSN 0947-8396. 27

24 *Journal of laser applications*, AMER INST PHYSICS, v. 10, p. 18–28. ISSN 1042-346X. 27, 31, 32

25 ZAVESTOVSKAYA, I. N. et al. Analysis of the nonlinear absorption mechanisms in ablation of transparent materials by high-intensity and ultrashort laser pulses. *Applied physics. A, Materials science processing*, Springer-Verlag, Berlin/Heidelberg, v. 92, n. 4, p. 903–906, 2008. ISSN 0947-8396. 28

26 ZHANG, Z. et al. Mechanisms of femtosecond laser ablation of ni3al: Molecular dynamics study. *Optics and laser technology*, Elsevier Ltd, OXFORD, v. 133, p. 106505, 2021. ISSN 0030-3992. 30

27 HEBERLE, J. et al. Ultrashort pulse laser cutting of intraocular lens polymers. *Journal of laser micro nanoengineering*, JAPAN LASER PROCESSING SOC, OSAKA, v. 9, n. 2, p. 103–107, 2014. ISSN 1880-0688. 31

28 LIPPERT, T. Laser application of polymers. *Polymers and Light*, Springer Berlin Heidelberg, Berlin, Heidelberg, v. 168, p. 51–246, 2004. ISSN 0065-3195. 31

29 PHAM, D. et al. Effects of polymer properties on laser ablation behaviour. *Smart materials and structures*, IOP Publishing, BRISTOL, v. 11, n. 5, p. 668–674, 2002. ISSN 0964-1726. 31

30 CHIAVERINI, V. Tecnologia mecânica: materiais de construção mecânica. *McGraw-Hill*, v. 2, p. 250–258, 1986. 32

31 KARTHIK, P.; SINGH, S. P. et al. Copper conductive inks: synthesis and utilization in flexible electronics. *RSC advances*, Royal Society of Chemistry, v. 5, n. 79, p. 63985–64030, 2015. 32

32 SILVA, L. A. et al. Cobre: produção industrial e aplicações. *Química Nova*, SciELO Brasil, v. 42, p. 1154–1161, 2020. 32

33 BI, G. et al. Evaluation of uncertainty in determining average grain size by astm e112 standard. In: IOP PUBLISHING. *IOP Conference Series: Materials Science and Engineering*. [S.l.], 2020. v. 733, n. 1, p. 012045. 34

34 DEDAVID, B. A.; GOMES, C. I.; MACHADO, G. *Microscopia eletrônica de varredura: aplicações e preparação de amostras: materiais poliméricos, metálicos e semicondutores*. [S.l.]: EdiPUCRS, 2007. 35

35 KESTENBACH, H.-J.; FILHO, W. J. B. Microscopia eletrônica: transmissão e varredura. *São Paulo: ABM*, 1994. 35

36 TATA, B.; RAJ, B. Confocal laser scanning microscopy: Applications in material science and technology. *Bulletin of Materials Science*, Springer, v. 21, n. 4, p. 263–278, 1998. 36

37 PADDOCK, S. W. Confocal laser scanning microscopy. *Biotechniques*, Future Science, v. 27, n. 5, p. 992–1004, 1999. 36

6 Appendix

6.1 Appendix 1

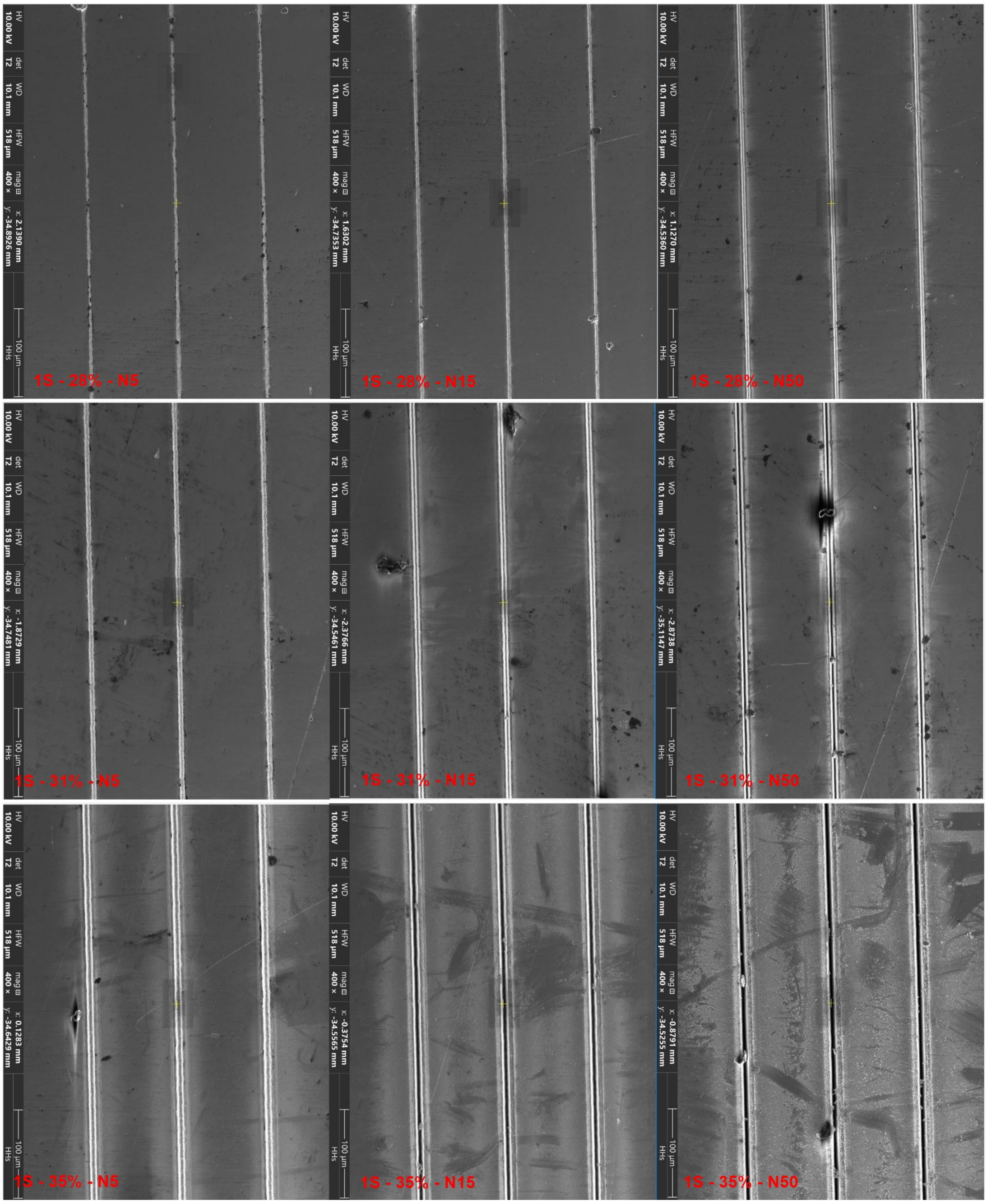

Figure 32 – SEM analysis containing an overview of all ablated lines for each power and number of repetitions of the 1S sample.

6.2 Appendix 2

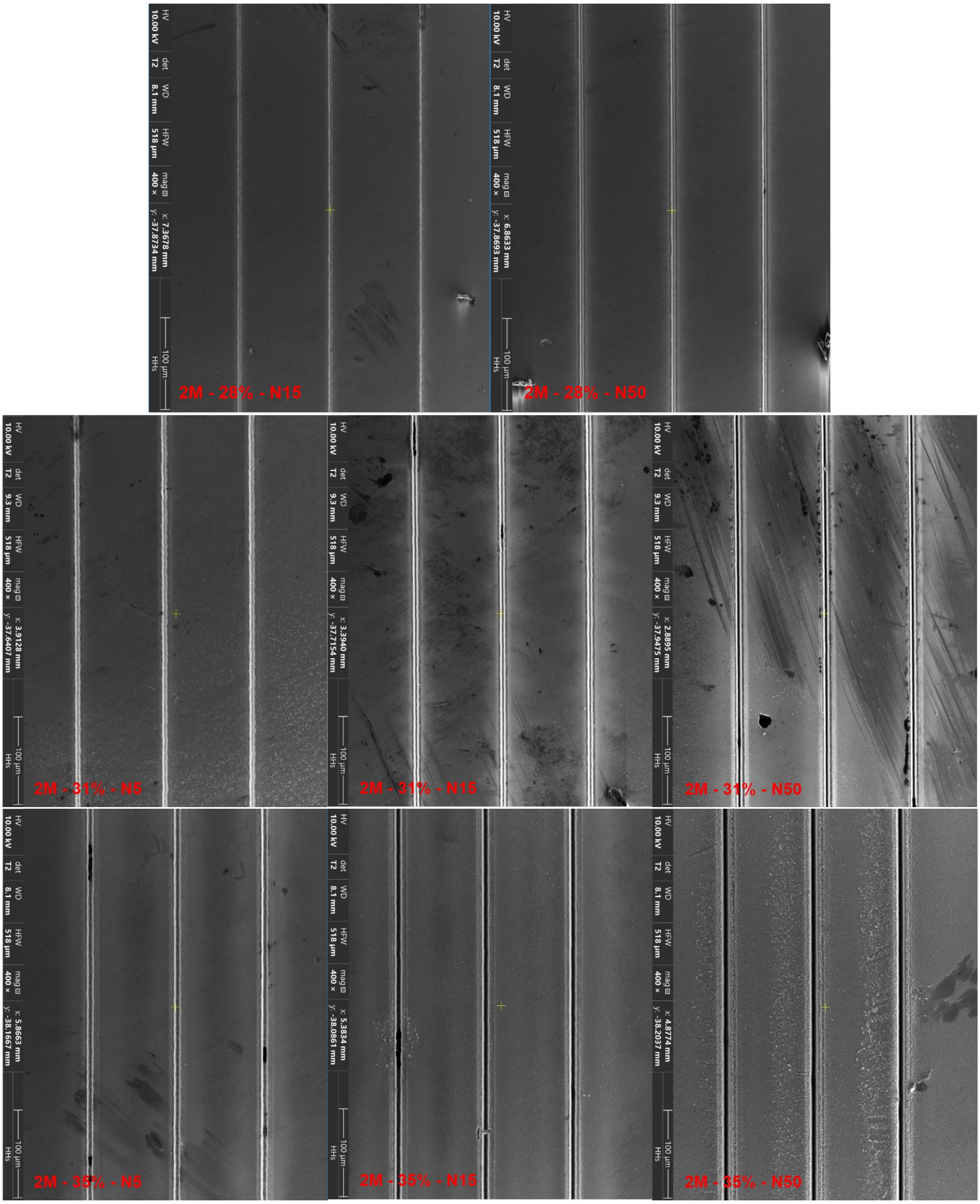

Figure 33 – SEM analysis containing an overview of all ablated lines for each power and number of repetitions of the 2M sample.

6.3 Appendix 3

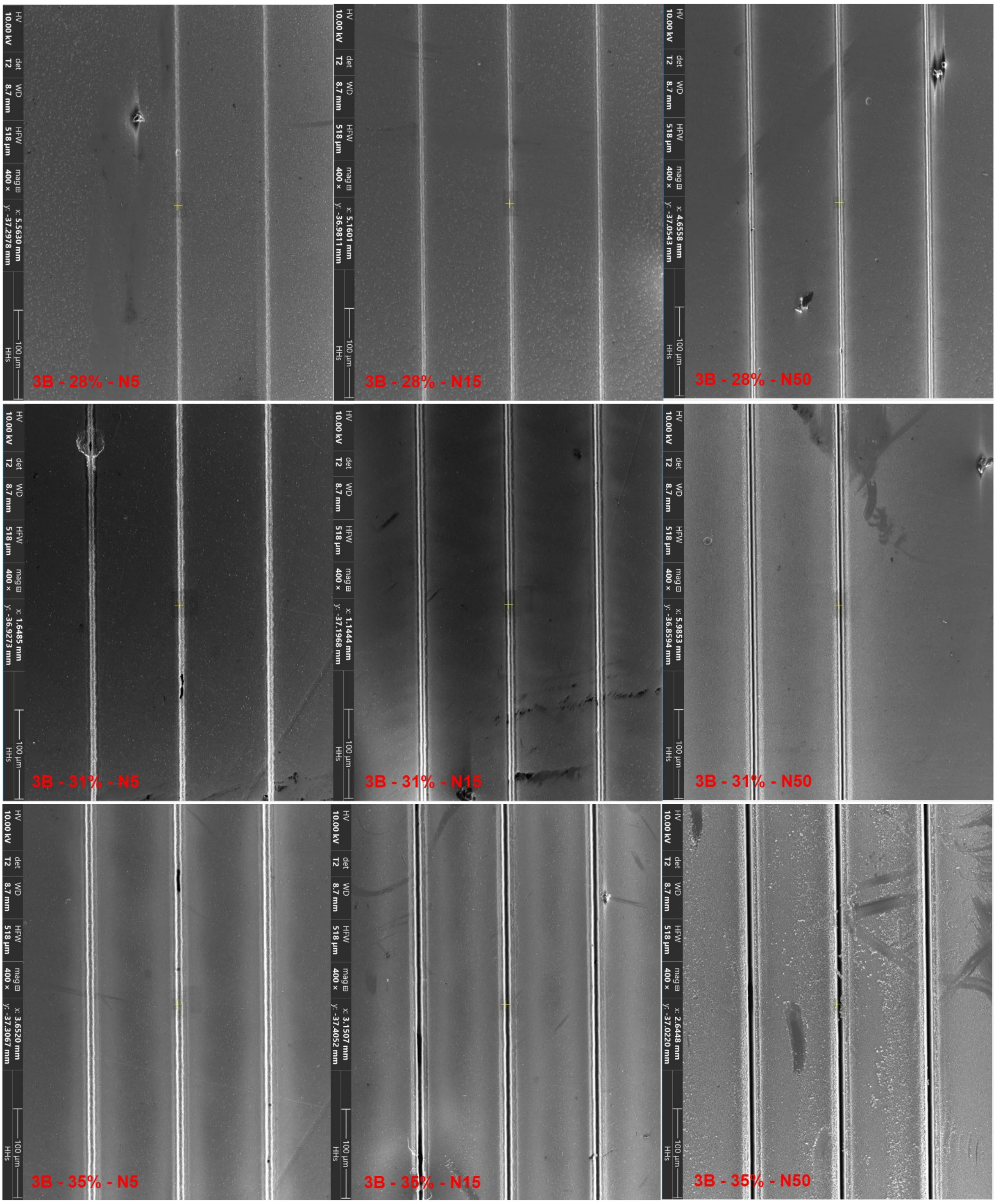

Figure 34 – SEM analysis containing an overview of all ablated lines for each power and number of repetitions of the 3B sample.

6.4 Appendix 4

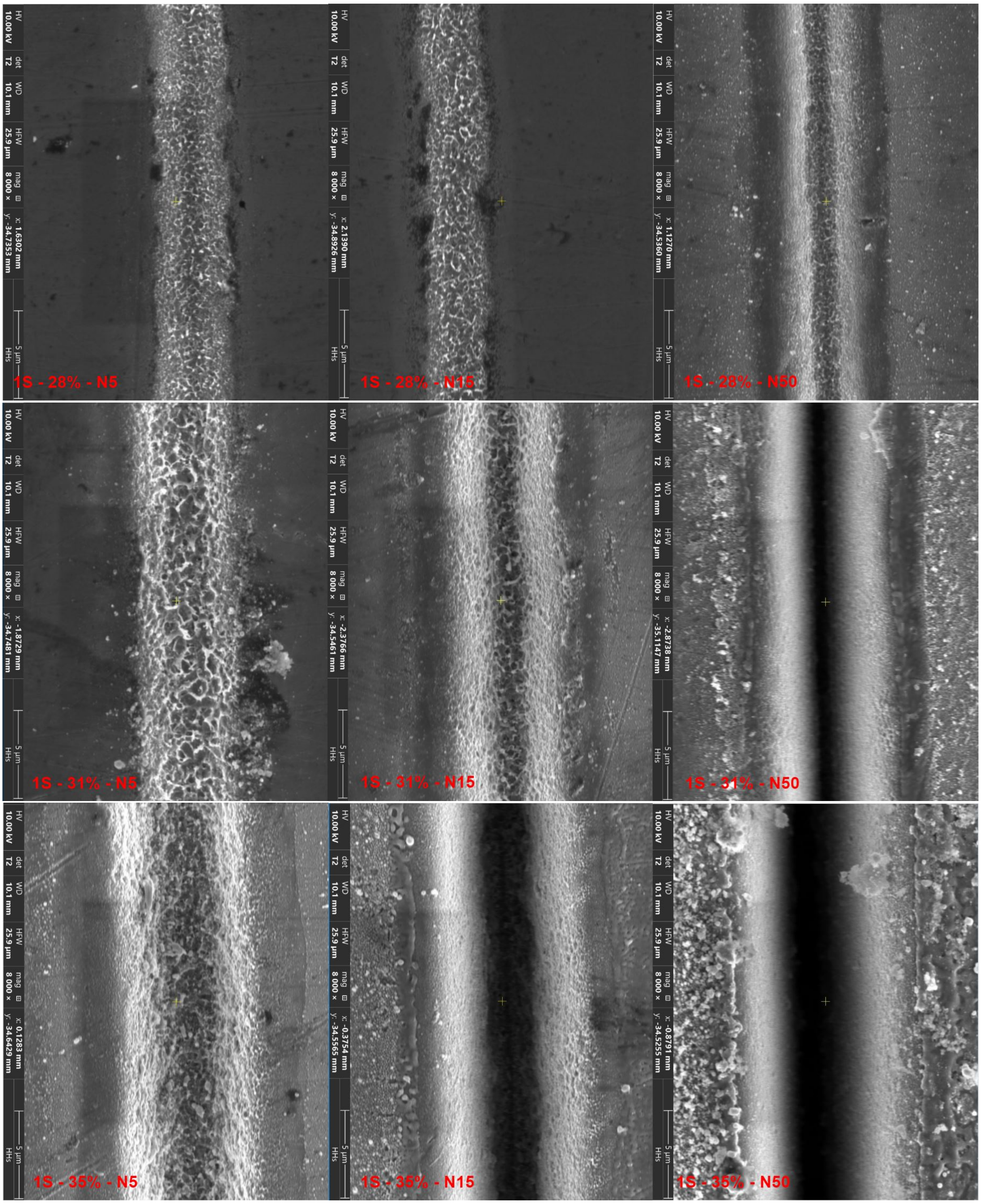

Figure 35 – Extended SEM analyses on a single ablation line for each power and number of repetitions of the 1S sample.

6.5 Appendix 5

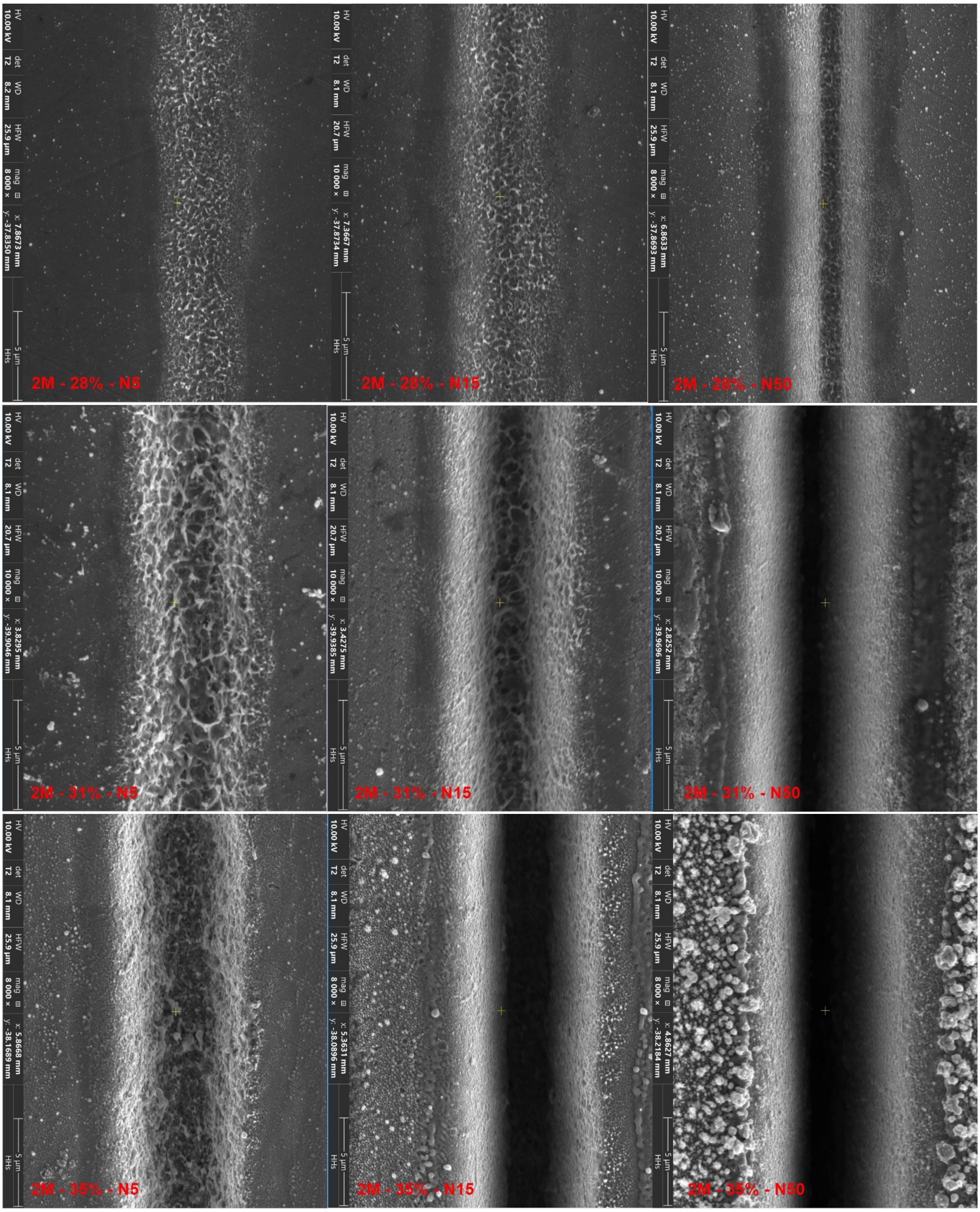

Figure 36 – Extended SEM analyses on a single ablation line for each power and number of repetitions of the 2M sample.

6.6 Appendix 6

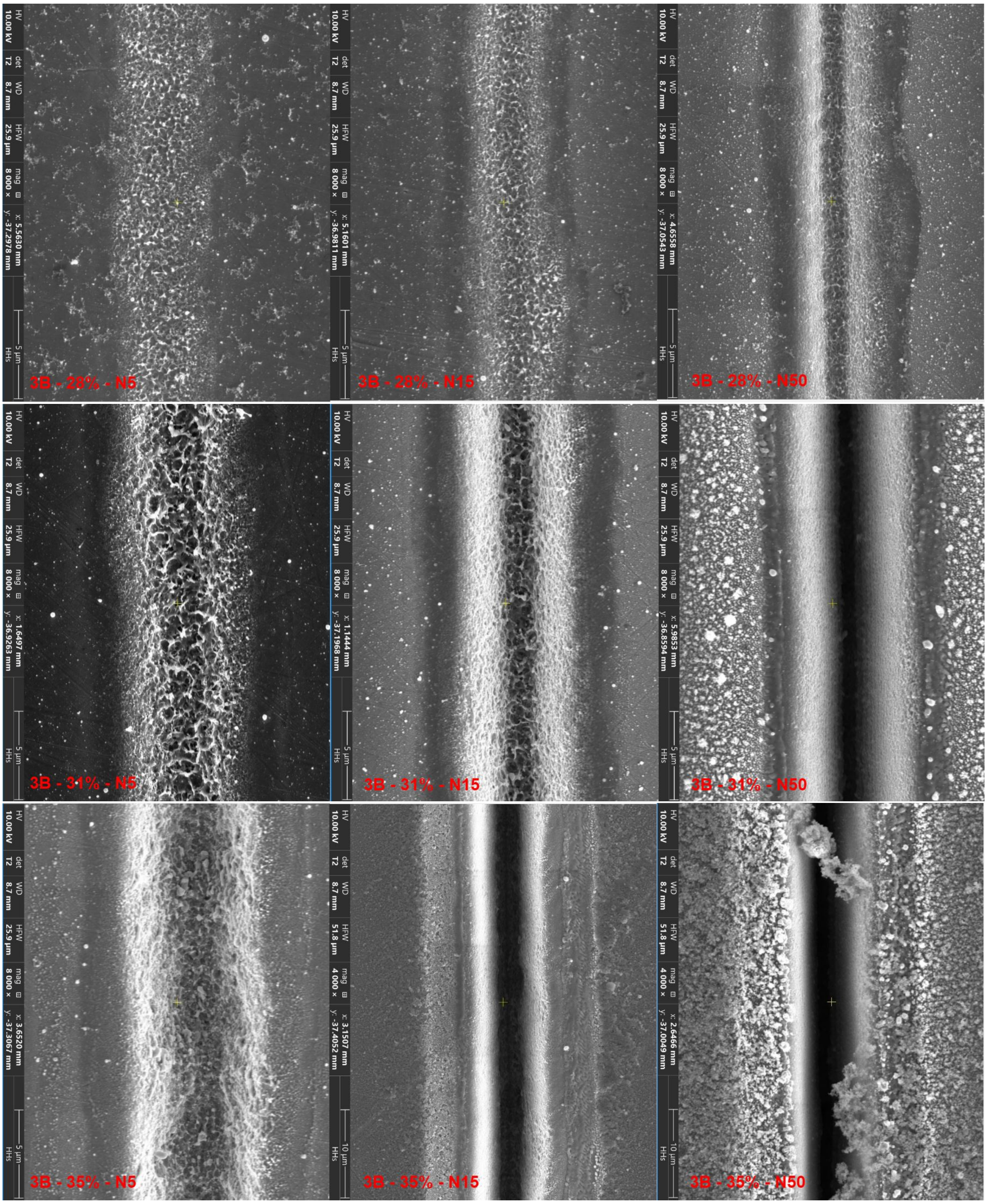

Figure 37 – Extended SEM analyses on a single ablation line for each power and number of repetitions of the 3B sample.

6.7 Appendix 7

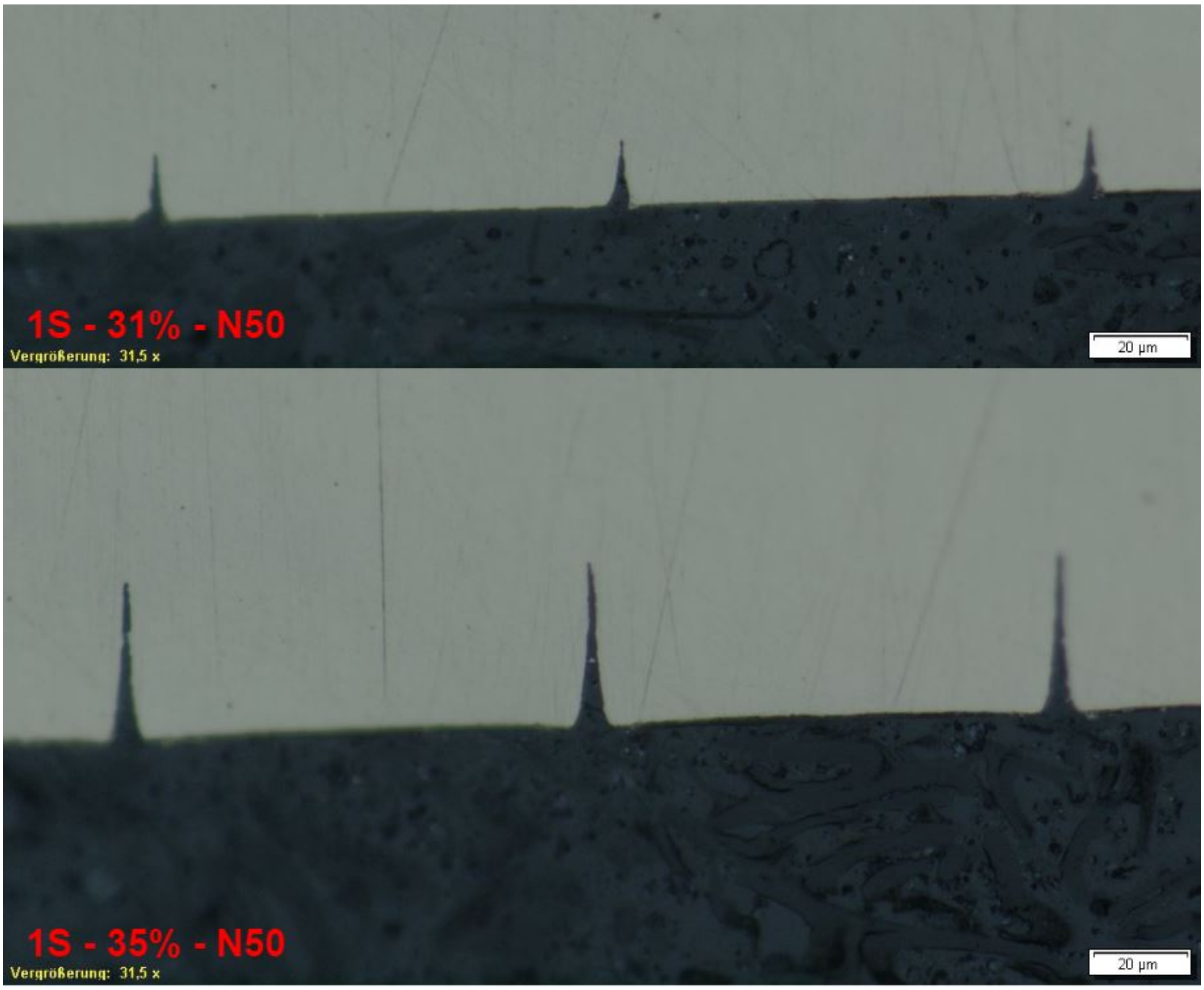

Figure 38 – Cross section images of the ablated profile of sample 1S obtained by optical microscopy.

6.8 Appendix 8

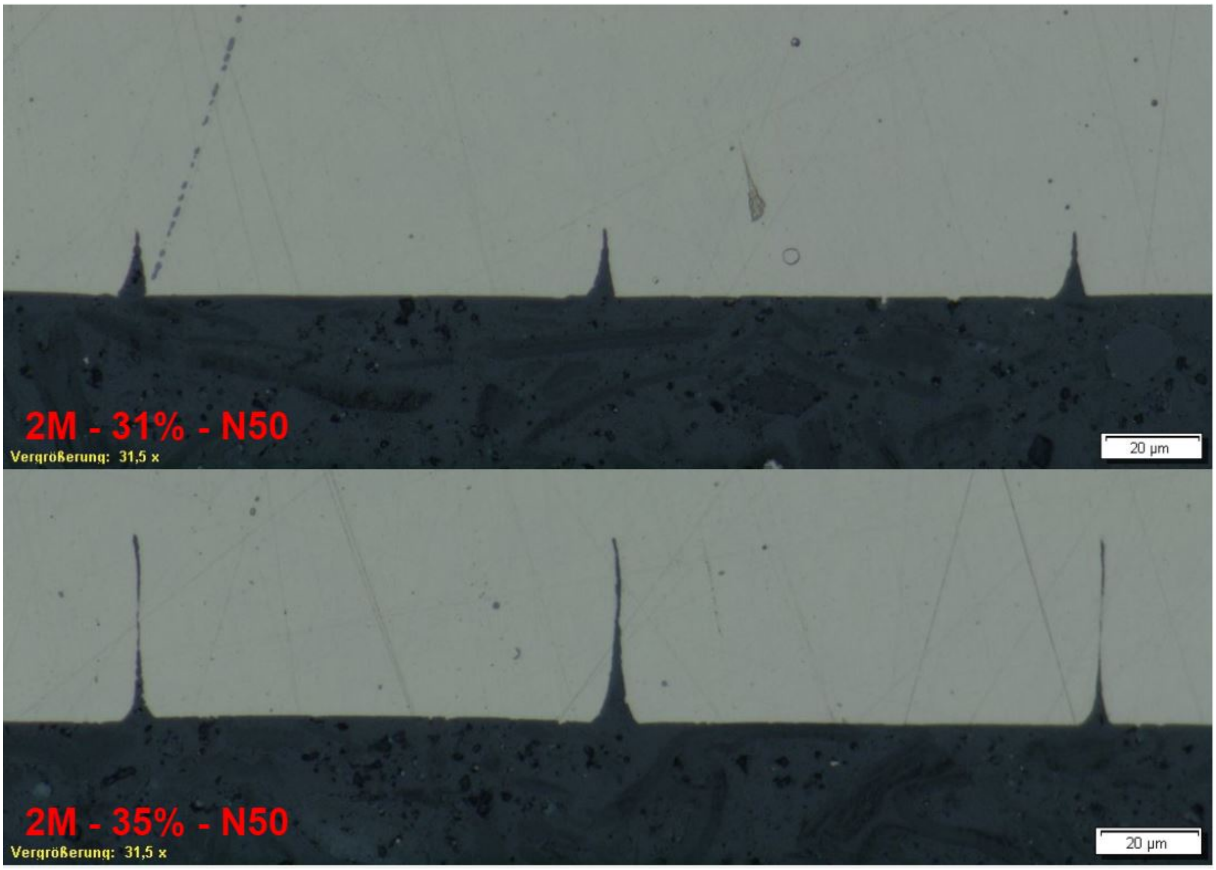

Figure 39 – Cross section images of the ablated profile of sample 2M obtained by optical microscopy.

6.9 Appendix 9

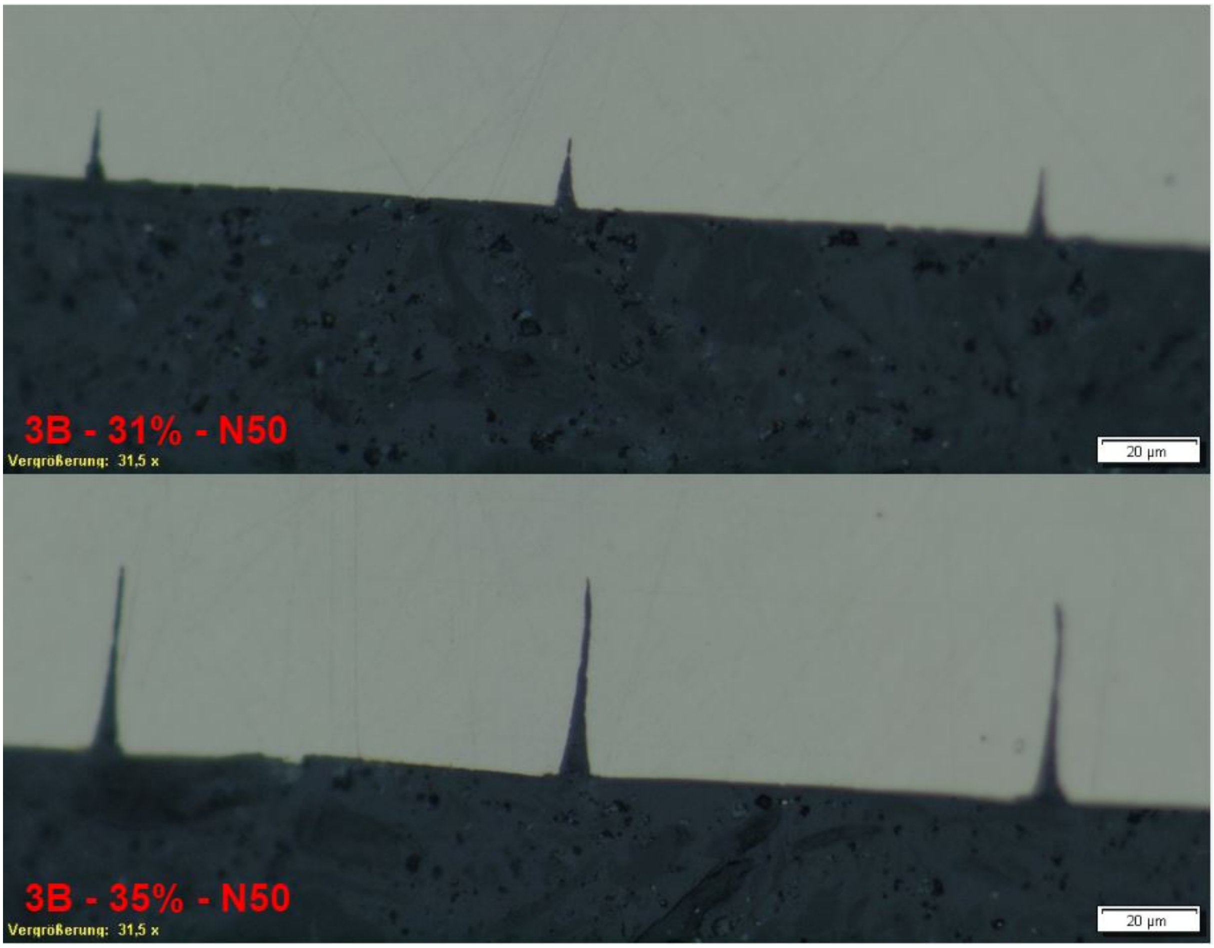

Figure 40 – Cross section images of the ablated profile of sample 3B obtained by optical microscopy.